NASA

TECHNICAL MEMORANDUM

X-582

EFFECTS OF NOSE-CONE ANGLE ON THE TRANSONIC AERODYNAMIC

CHARACTERISTICS OF A BLUNT CONE-CYLINDER BODY HAVING

A CYLINDRICAL, FLARED, OR BLUNT-FINNED AFTERBODY

By Stuart L. Treon

Ames Research Center
Moffett Field, Calif.

Dated

NATIONAL AERONAUTICS AND SPACE ADMINISTRATION

WASHINGTON   October 1961

:: DECLASSIFIED

NATIONAL AERONAUTICS AND SPACE ADMINISTRATION

TECHNICAL MEMORANDUM X-582

EFFECTS OF NOSE-CONE ANGLE ON THE TRANSONIC AERODYNAMIC

CHARACTERISTICS OF A BLUNT CONE-CYLINDER BODY HAVING

A CYLINDRICAL, FLARED, OR BLUNT-FINNED AFTERBODY*

By Stuart L. Treon

SUMMARY

An investigation has been conducted in a transonic wind tunnel to determine the static aerodynamic characteristics of a body of revolution having rounded nose cones of various angles and a cylindrical, flared, or blunt-finned afterbody. The nose-cone half-angle was varied from 14° to 45°. Data are presented for angles of attack from -2° to $+14^\circ$ and at Mach numbers from 0.6 to 1.4. The test Reynolds number was either 0.375 or 0.50 million based on the cylindrical body diameter.

INTRODUCTION

Demand for aerodynamic data for low-fineness-ratio bodies of revolution at transonic speeds stems not only from interest in atmosphere-entry vehicles, but also from an awareness that the stability of such bodies can vary greatly in the transonic speed range. The present report is one of a series presenting the results of an investigation conducted at the Ames Research Center to determine the effects of systematic changes in model geometry on the aerodynamic characteristics of low-fineness-ratio bodies at transonic speeds. Previous phases of the investigation are reported in references 1 through 6. In the present report are the results of an investigation of the effects of nose-cone angle on the static aerodynamic characteristics of a blunt-nosed, low-fineness-ratio body of revolution having a cylindrical, flared or blunt-finned afterbody. The half-angle of the nose cones was varied from 14° to 45°.

The results are presented without detailed discussion.

---

*Title, Unclassified

NOTATION

B   model base area

C_A measured axial force coefficient, $\dfrac{\text{measured axial force}}{qS}$

C_{A_b} base axial force coefficient, $\dfrac{(p_\infty - p_b)B}{qS}$

C_{A_f} forebody axial force coefficient, $C_A - C_{A_b}$

C_m pitching-moment coefficient about the nose-body juncture, $\dfrac{\text{pitching moment}}{qSd}$

$\dfrac{C_m}{\alpha}$ slope of a straight line drawn from C_m at $\alpha = 0^\circ$ to any point on the C_m vs. α curve

C_N normal force coefficient, $\dfrac{\text{normal force}}{qS}$

$\dfrac{C_N}{\alpha}$ slope of a straight line drawn from C_N at $\alpha = 0^\circ$ to any point on the C_N vs. α curve

c.p.   center-of-pressure location in body diameters, positive when forward of the nose-body juncture, $\dfrac{C_m/\alpha}{C_N/\alpha}$

d   cylindrical-body diameter

M   Mach number

p_b base pressure

p_∞ test-section static pressure

q   dynamic pressure

S   cross-sectional area of cylindrical body

α angle of attack, deg

Model Component Designations

B_x cylindrical body, subscript denoting length in body diameters

C_{20} blunt, cruciform fins, leading-edge semivertex angle = 20°

F_{20-4} flared afterbody, semivertex angle = 20° and ratio of flare base
area to cylindrical body cross-sectional area = 4

N_x nose, subscript denoting number in series (see fig. 1 and ref. 4)

A
4
2
8

APPARATUS AND MODELS

The investigation was conducted in the Ames 2- by 2-Foot Transonic
Wind Tunnel, which is of the closed-circuit, variable-pressure type.
This facility (ref. 7) has a perforated test section which permits con-
tinuous, choke-free operation from subsonic speeds to Mach number 1.4.

The configurations investigated were combinations of four rounded
nose cones on a cylindrical body having three different afterbodies as
shown in figure 1. The nose-cone half-angle varied from 14° to 45°. The
afterbodies consisted of a cylinder, a 20° flare, and a cylinder with a
cruciform arrangement of blunt fins of 20° semivertex angle.

The models were mounted on a sting-supported strain-gage balance
encased in a metal shroud as shown in figure 1. Representative photo-
graphs of the models installed in the test section are shown in figure 2.

TESTS AND DATA REDUCTION

Investigation of the aerodynamic forces and moments was conducted at
Mach numbers from 0.6 to 1.4 at angles of attack from approximately -2^O
to $+14^O$. The procedure for traversing the angle-of-attack range was
predicated on the possible occurrence of flow hysteresis of the type
described in reference 8 and observed in previously reported phases of
the present investigation (refs. 3, 4, and 5). At all test Mach numbers,
the angle of attack was decreased from 0° to -2^O, then increased progres-
sively to 14°. At Mach numbers greater than 0.90, the angle of attack
was decreased from 14° to -2^O to encompass possible hysteresis loops.
The Reynolds number based on the cylindrical body diameter was 0.375
million for the models with the 14° half-angle nose cone and was 0.50
million for all of the other models. Additional runs were made at a
Reynolds number of 0.5 million to obtain shadowgraphs at selected Mach
numbers and angles of attack.

To restrict the variation of boundary-layer transition location, boundary-layer trip wires were placed on the noses of the models as shown in figure 1. The effectiveness of the trip wires was determined from flow-visualization studies employing the technique of reference 9. For all models, the boundary layer was observed to be turbulent ahead of or in the region of the trip wires.

The axial forces were resolved into forebody and base coefficients. For the forebody coefficients, the measured axial forces were adjusted to account for the difference between the measured base pressures and an assumed condition of free-stream static pressure acting over the entire base area of each model.

The results of reference 10 for models with cylindrical afterbodies and of reference 11 for models with flared afterbodies indicate that the presence of the sting may have a significant effect on base axial force. However, there is evidence in references 8 and 10 that the forebody axial force is not significantly affected. The magnitude of the sting interference on the base axial force is not known for the present models.

The angles of attack have been corrected for elastic deflection of the balance and sting under aerodynamic loads. Stream angularity corrections are negligible.

No corrections have been made for possible interference effects of the perforated test section walls. Such interference effects are believed to be relatively small, in view of the results of tests at transonic speeds of various sizes of sharp- and blunt-nosed bodies reported in the appendix to reference 12.

In addition to the possible systematic errors from neglecting some of the above corrections, certain random errors exist which influence the precision, or repeatability, of the results. The precision of the data was determined by the method described in reference 13 and the average deviations of various quantities of this investigation were found to be approximately as follows:

M	± 0.003	C_m	± 0.03
α	$\pm 0.05^\circ$	C_{A_f}	± 0.02
C_N	± 0.02	C_{A_b}	± 0.01

RESULTS

The variations with angle of attack of coefficients of normal force, pitching moment, forebody axial force, and base axial force are presented in figures 3 through 6 for the various models of this investigation. Results are presented for both increasing and decreasing angles of attack where hysteresis loops or abrupt changes occurred in the variations of aerodynamic coefficients with angle of attack. The hysteresis phenomenon, which is associated with regions of separated flow, has been shown to be a common and undesirable feature of transonic flow over blunt-nosed bodies, since the introduction into the pitching cycle of the energy represented by the hysteresis loop may lead to large pitching oscillations (ref. 8).

The variations with Mach number of C_N/α and center-of-pressure location at three selected angles of attack are summarized in figures 7 and 8. Figure 9 presents the forebody and base axial force coefficients at 0° angle of attack over the test Mach number range.

Shadowgraph pictures are presented in figures 10 through 12 to show the effect of nose-cone angle on the flow over the various models.

Ames Research Center
National Aeronautics and Space Administration
Moffett Field, Calif., Aug. 21, 1961

REFERENCES

1. Knechtel, Earl D., Treon, Stuart L., and Wakefield, Roy M.: Transonic Static Aerodynamic Characteristics of a Blunt Cone-Cylinder Body With Flared Afterbody or Blunt Cruciform Fins. NASA TM X-40, 1959.

2. Wakefield, Roy M., Knechtel, Earl D., and Treon, Stuart L.: Transonic Static Aerodynamic Characteristics of a Blunt Cone-Cylinder Body With Flared Afterbodies of Various Angles and Base Areas. NASA TM X-106, 1959.

3. Knechtel, Earl D., Wakefield, Roy M., and Treon, Stuart L.: Transonic Static Aerodynamic Characteristics of a Low-Fineness-Ratio Body of Revolution Having a Blunt Ellipsoidal Nose and Flared Afterbodies of Various Angles and Base Areas. NASA TM X-113, 1959.

4. Treon, Stuart L., Wakefield, Roy M., and Knechtel, Earl D.: Effects of Nose Shape and Afterbody Flare on the Transonic Characteristics of a Low-Fineness-Ratio Body of Revolution. NASA TM X-164, 1960.

5. Wakefield, Roy M., Treon, Stuart L., and Knechtel, Earl D.: Effects of Centerbody Length and Nose Shape on the Transonic Characteristics of Low-Fineness-Ratio Bodies of Revolution With a Flared Afterbody. NASA TM X-366, 1960.

6. Treon, Stuart L., Wakefield, Roy M., and Knechtel, Earl D.: Effects of Spike-Mounted Flow Deflectors on the Transonic Aerodynamic Characteristics of a Blunt-Nosed Body of Revolution Having a Cylindrical or Flared Afterbody. NASA TM X-574, 1961.

7. Spiegel, Joseph M., and Lawrence, Leslie F.: A Description of the Ames 2- by 2-Foot Transonic Wind Tunnel and Preliminary Evaluation of Wall Interference. NACA RM A55I21, 1956.

8. Reese, David E., Jr., and Wehrend, William R., Jr.: An Investigation of the Static and Dynamic Aerodynamic Characteristics of a Series of Blunt-Nosed Cylinder-Flare Models at Mach Numbers From 0.65 to 2.20. NASA TM X-110, 1959.

9. Main-Smith, J.D.: Chemical Solids as Diffusible Coating Films for Visual Indications of Boundary-Layer Transition in Air and Water. R and M No. 2755, British, A.R.C., 1954.

10. Lee, George, and Summers, James L.: Effects of Sting-Support Interference on the Drag of an Ogive-Cylinder Body With and Without a Boattail at 0.6 to 1.4 Mach number. NACA RM A57I09, 1957.

11. Reese, David E., Jr., and Wehrend, William R., Jr.: Effects of Sting-Support Interference on the Base Pressures of a Model Having a Blunt-Nosed Cylinder Body and a Conical Flare at Mach Numbers from 0.65 to 2.20. NASA TM X-161, 1960.

12. Treon, Stuart L.: The Effect of Nose Shape on the Static Aerodynamic Characteristics of Ballistic-Type Missile Models at Mach Numbers From 0.6 to 1.4. NASA Memo 5-17-59A, 1959.

13. Beers, Yardley: Introduction to the Theory of Error. Addison-Wesley Pub. Co., Cambridge, Mass., 1953.

A
4
2
8
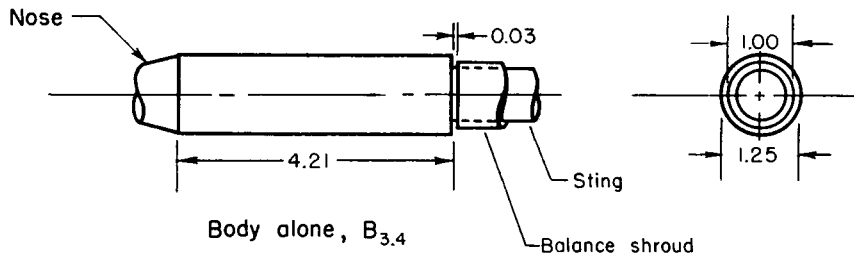
Note:

Dimensions in inches

Nose

0.03

Sting

Balance shroud

1.00

1.25

4.21

Body alone, B$_{3.4}$

20°

1.25

2.50

2.50

1.71

Body with flare, B$_2$F$_{20-4}$

20°

14°

4°30'

0.125 R

1.25

2.50

2.50

1.71
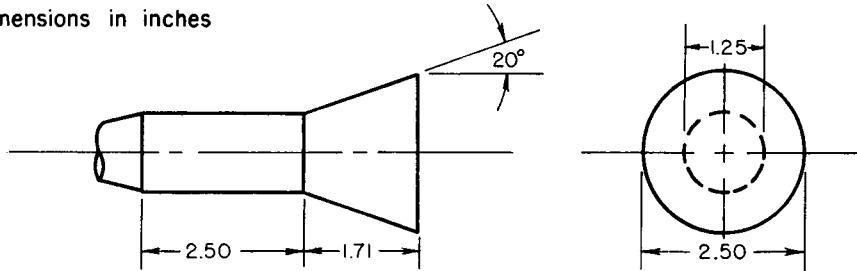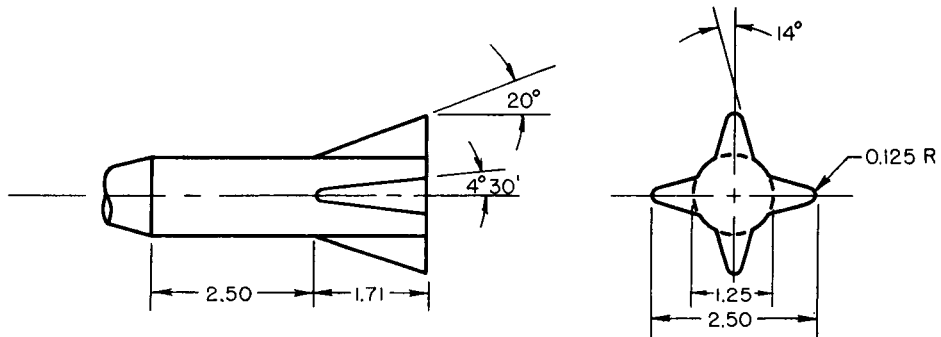
Body with cruciform fins, B$_2$C$_{20}$

0.008 diam.
trip wire

1.02

14°

0.312 R

1.52

Nose, N$_2$

0.71

20°

0.312 R

1.12

Nose, N$_3$

0.45

30°

0.312 R

0.77

Nose, N$_4$

0.26

45°

0.312 R

0.50

Nose, N$_5$
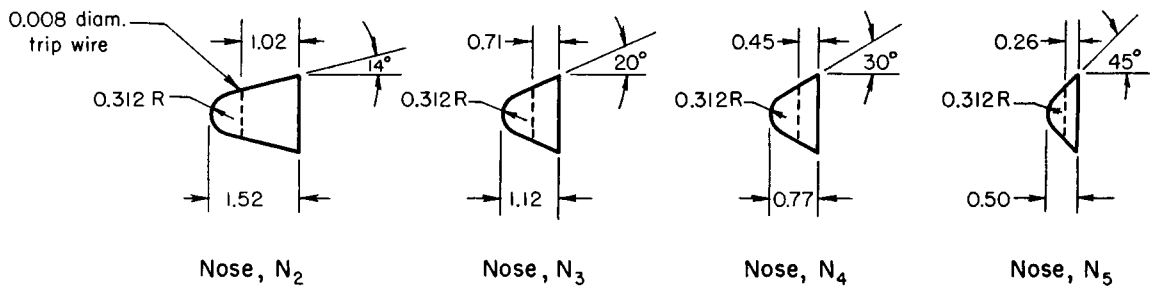
Figure 1.- Sketches and dimensions of model components.
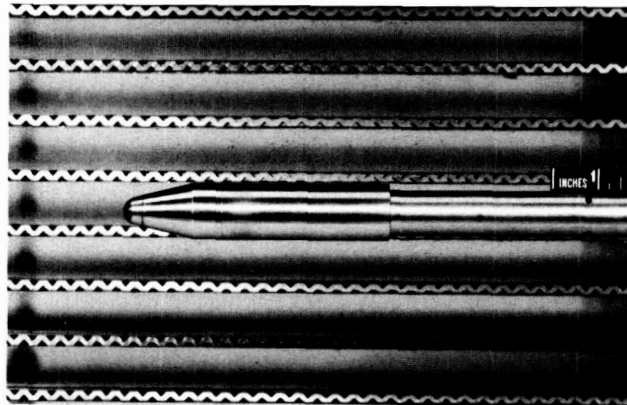
$N_2B_{3.4}$ A-24673
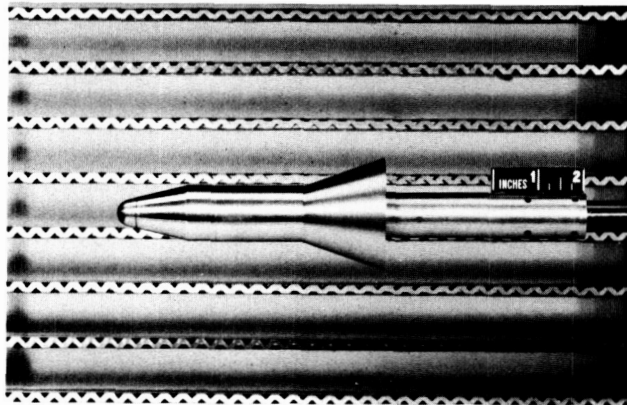
$N_2B_2F_{20-4}$ A-24665
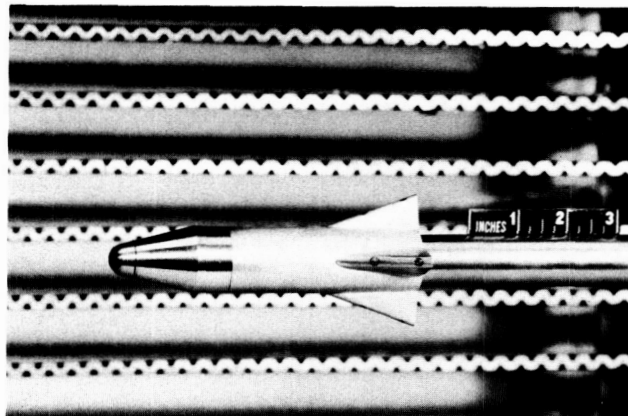
$N_2B_2C_{20}$ A-24676

Figure 2.- Models installed in the test section of the Ames 2- by 2-Foot Transonic Wind Tunnel.
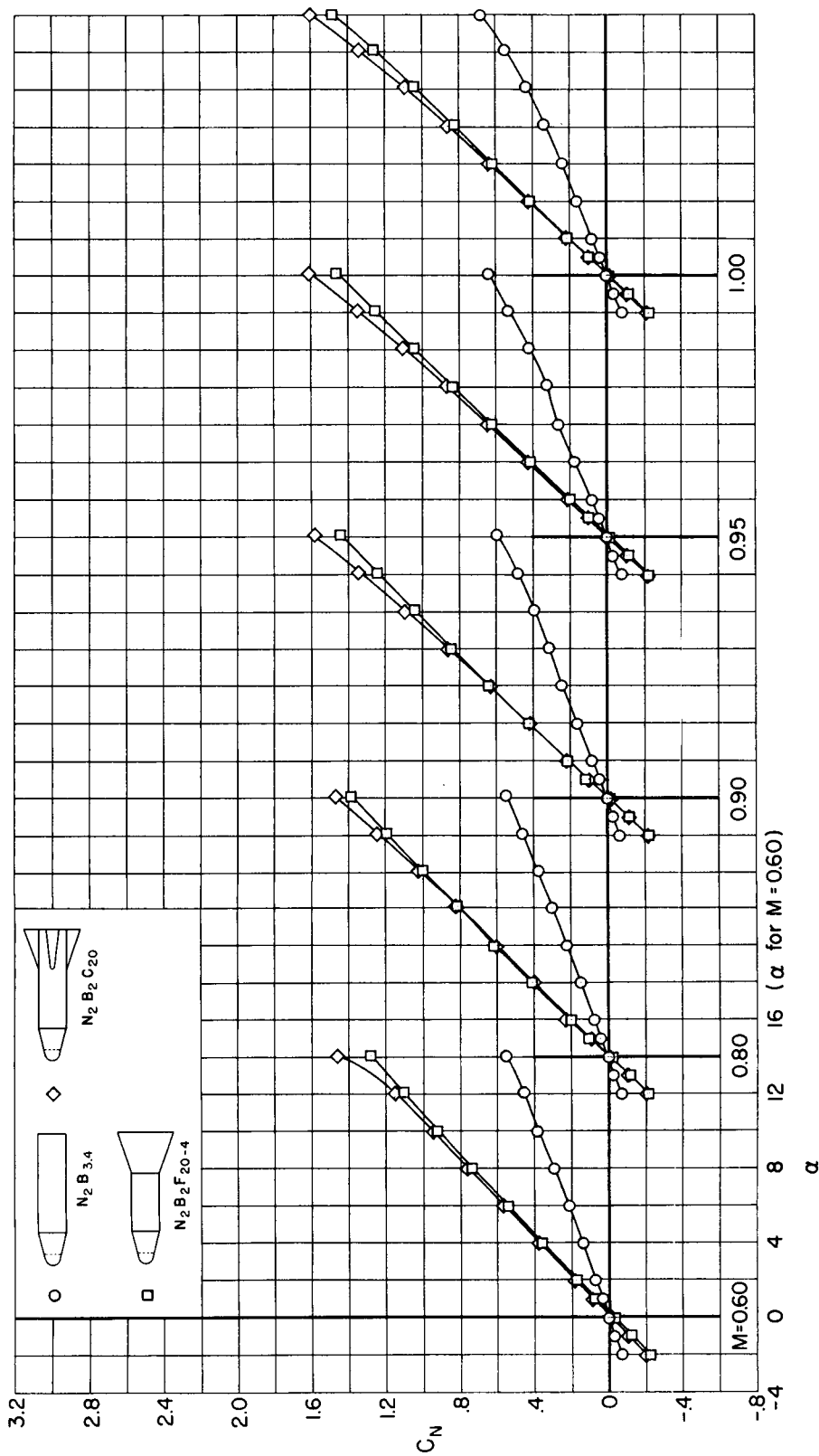
(a) Normal-force coefficient; M = 0.60 to 1.00.

Figure 3.- Static longitudinal aerodynamic coefficients for models with the N_2 nose.
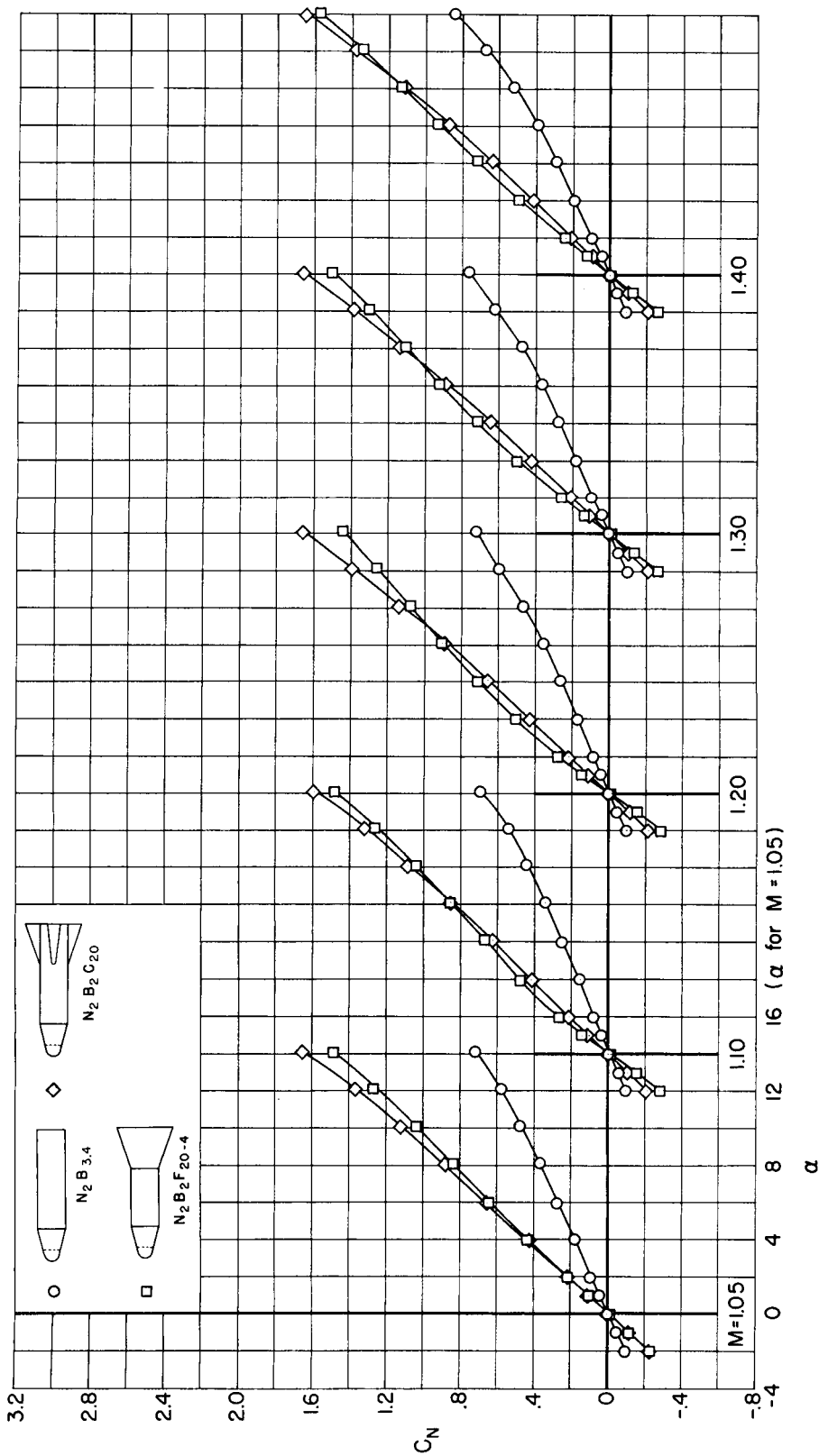
(b) Normal-force coefficient; M = 1.05 to 1.40.
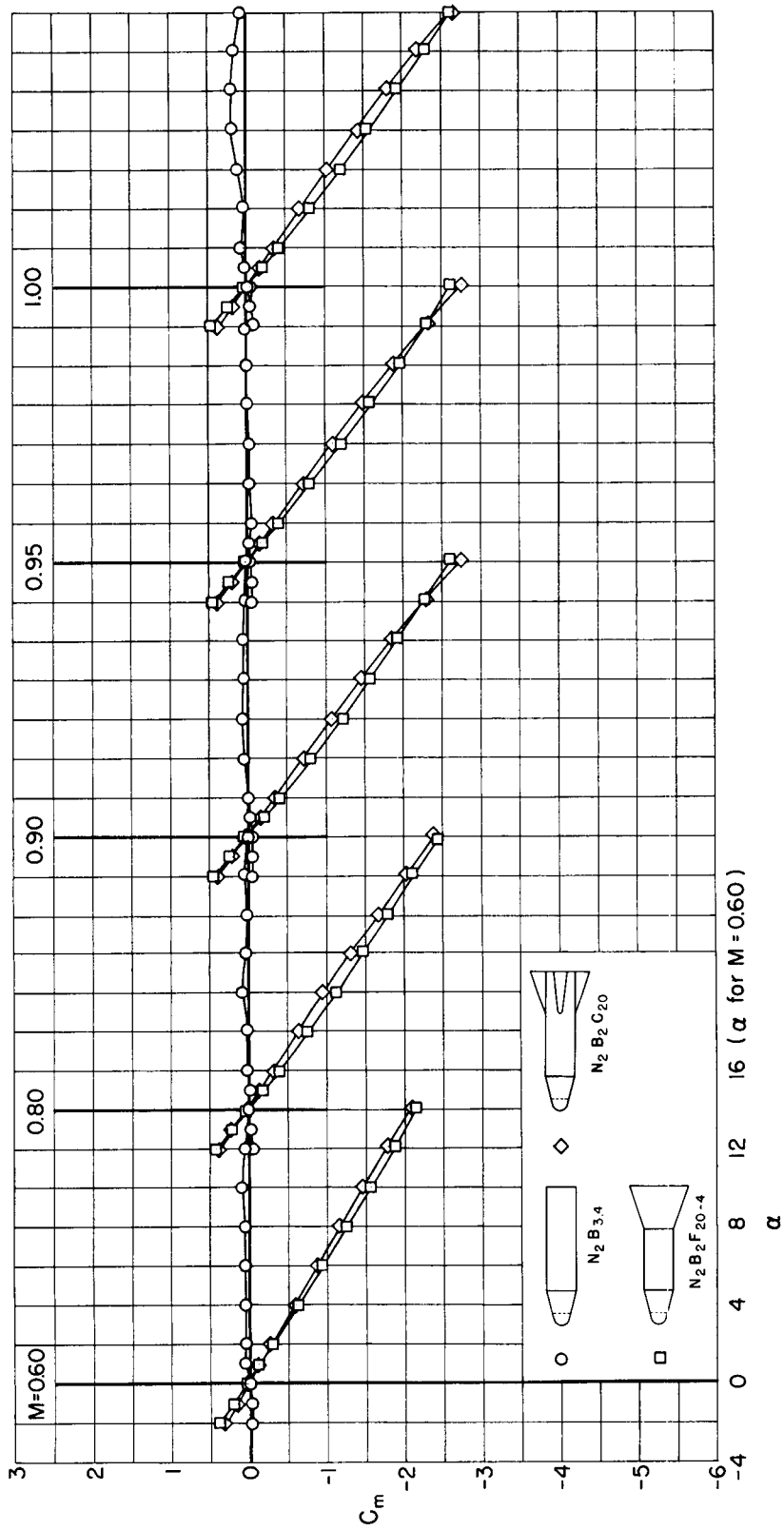
Figure 3.- Continued.

(c) Pitching-moment coefficient; M = 0.60 to 1.00
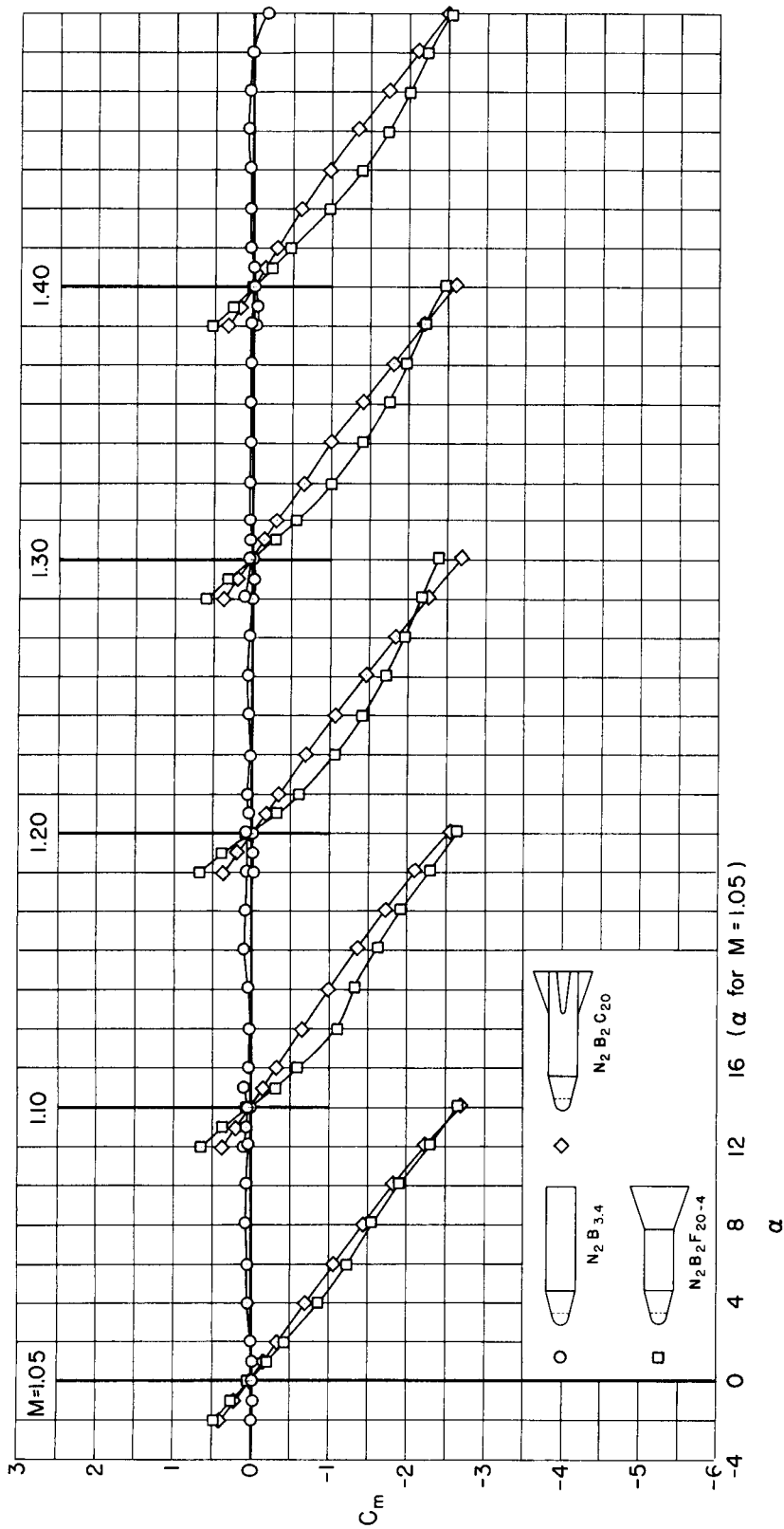
Figure 3.- Continued.

(d) Pitching-moment coefficient; M = 1.05 to 1.40
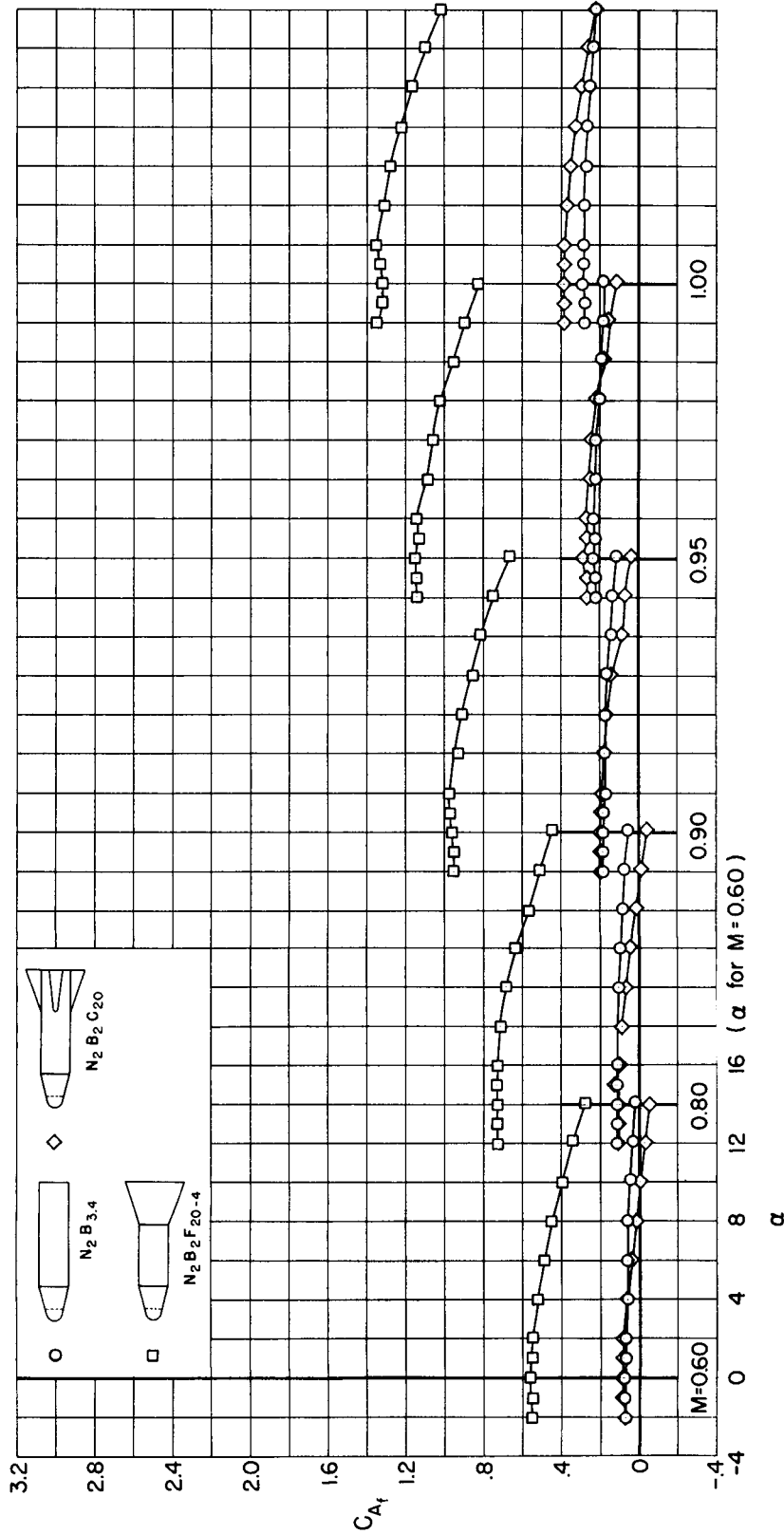
Figure 3.- Continued.

(e) Forebody axial-force coefficient; M= 0.60 to 1.00.
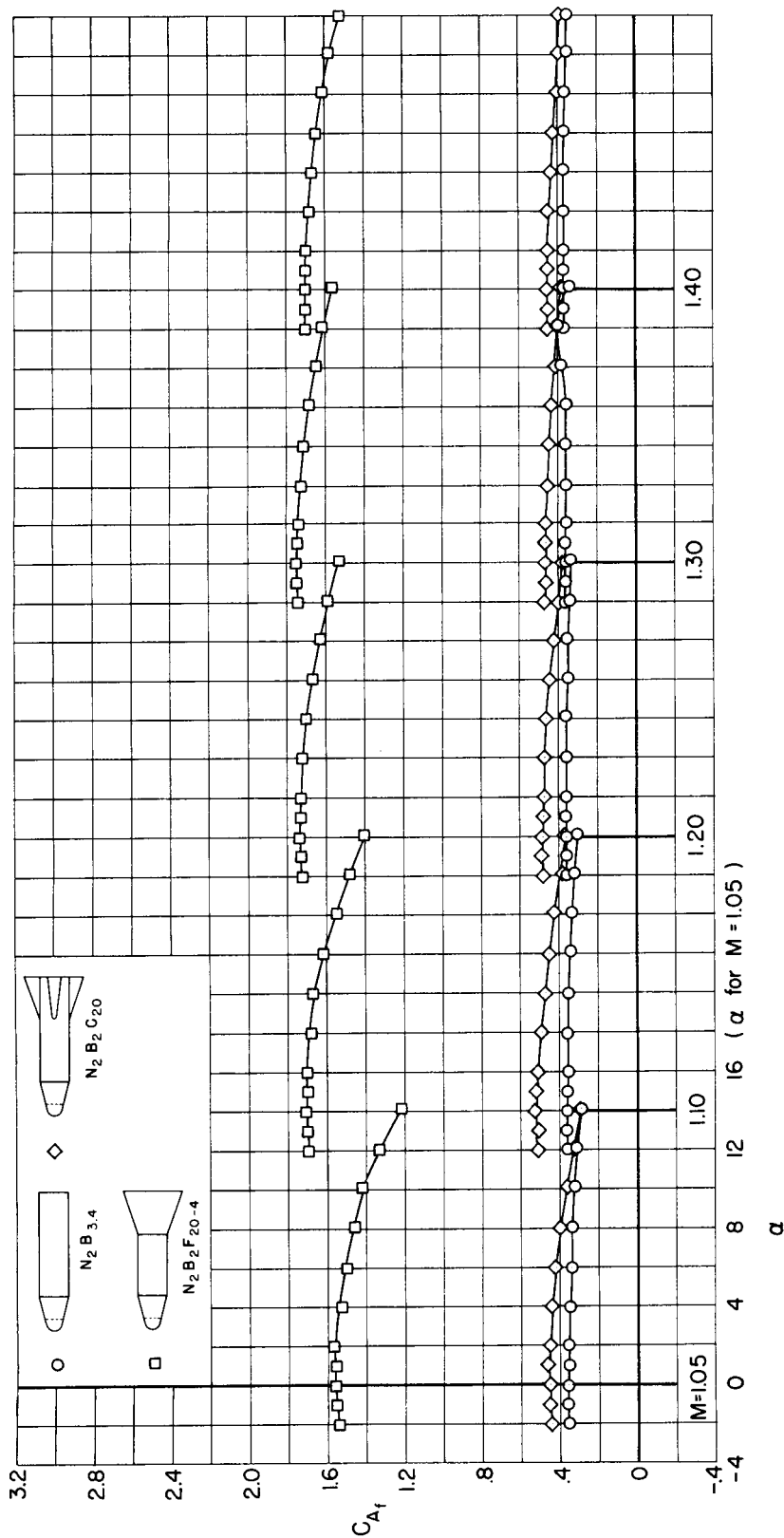
Figure 3.- Continued.

(f) Forebody axial-force coefficient; M = 1.05 to 1.40.
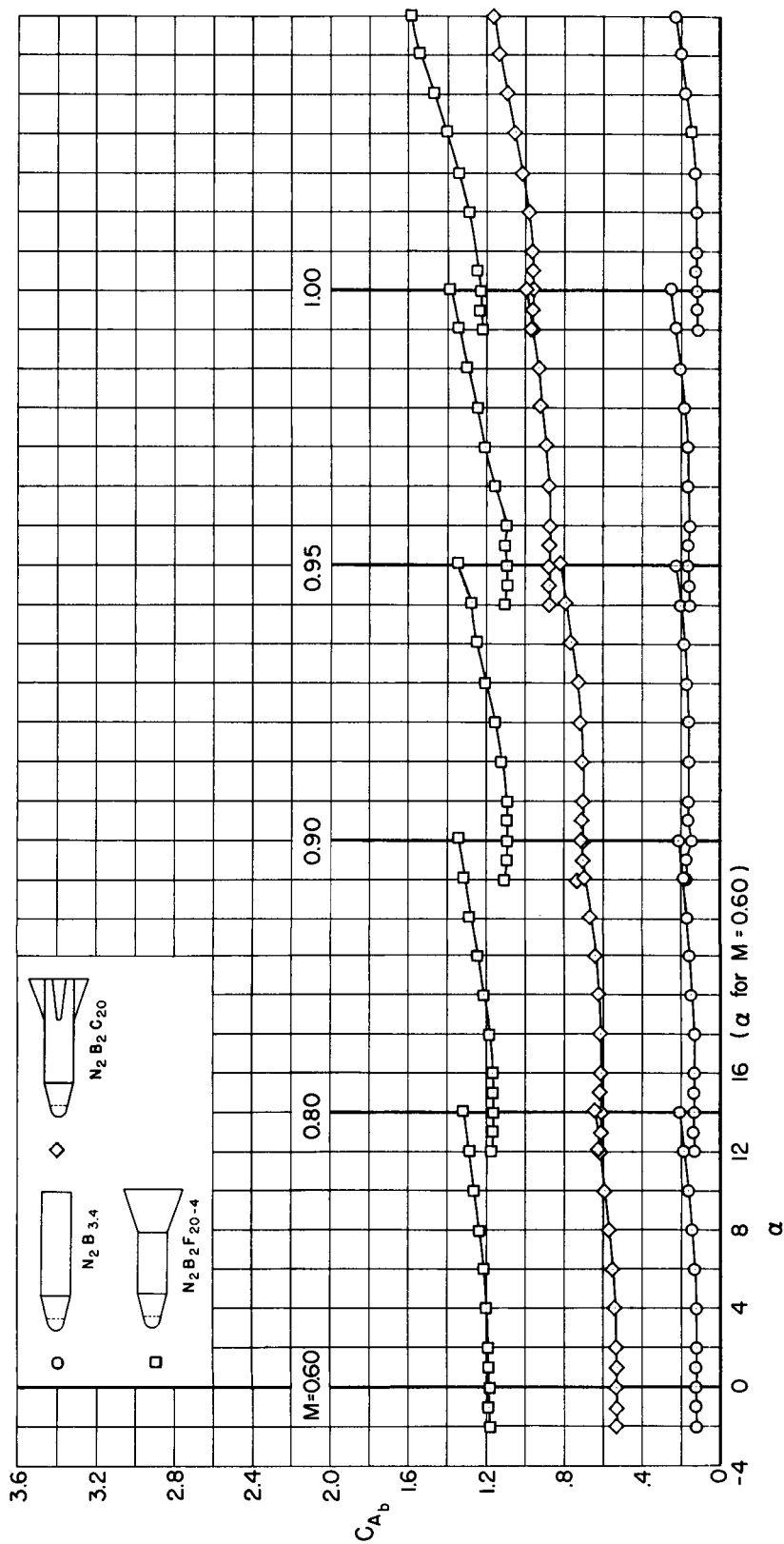
Figure 3.- Continued.

(g) Base axial-force coefficient; M = 0.60 to 1.00.

Figure 3.- Continued.
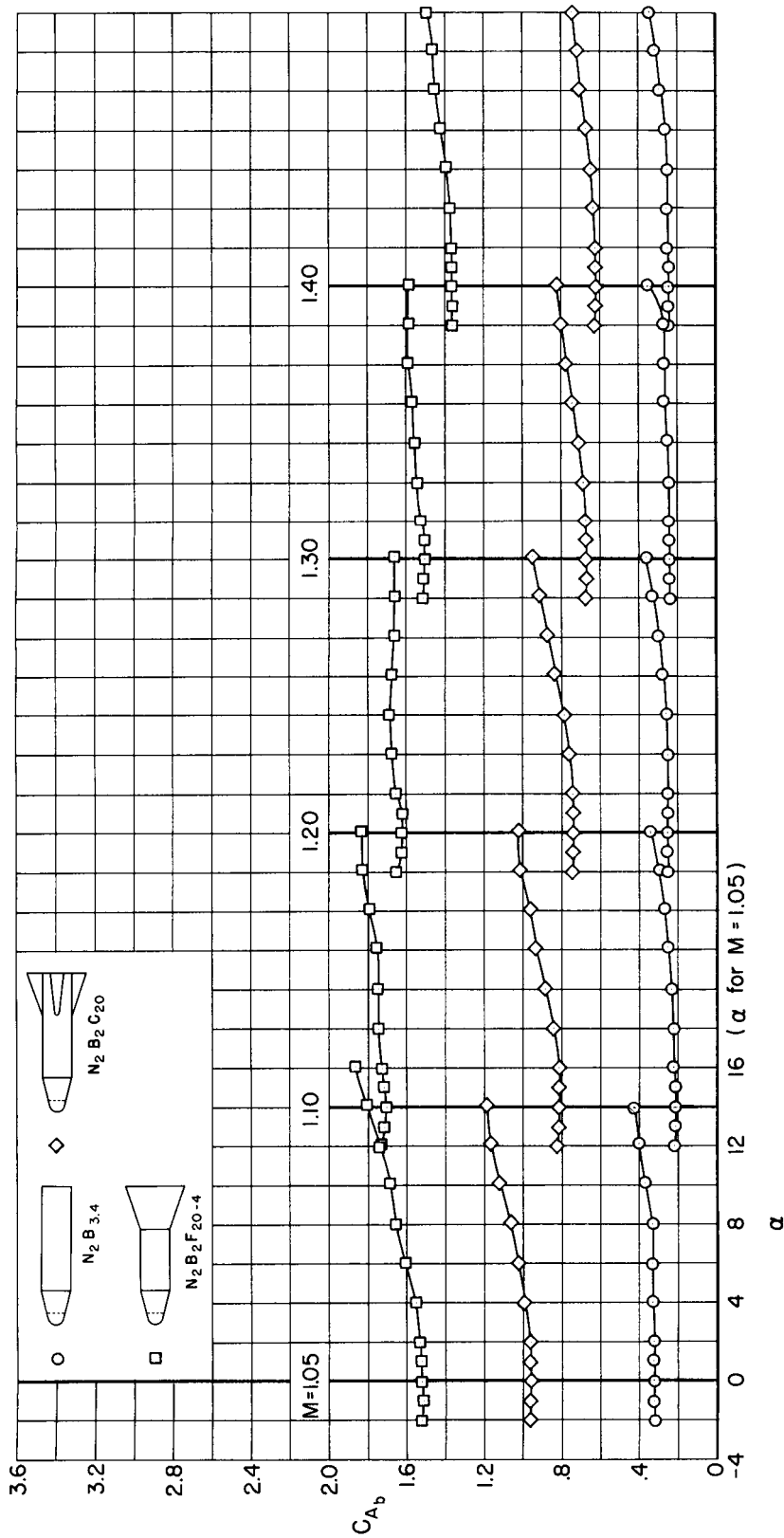
(h) Base axial-force coefficient; M = 1.05 to 1.40

Figure 3.- Concluded.

A
4
2
8
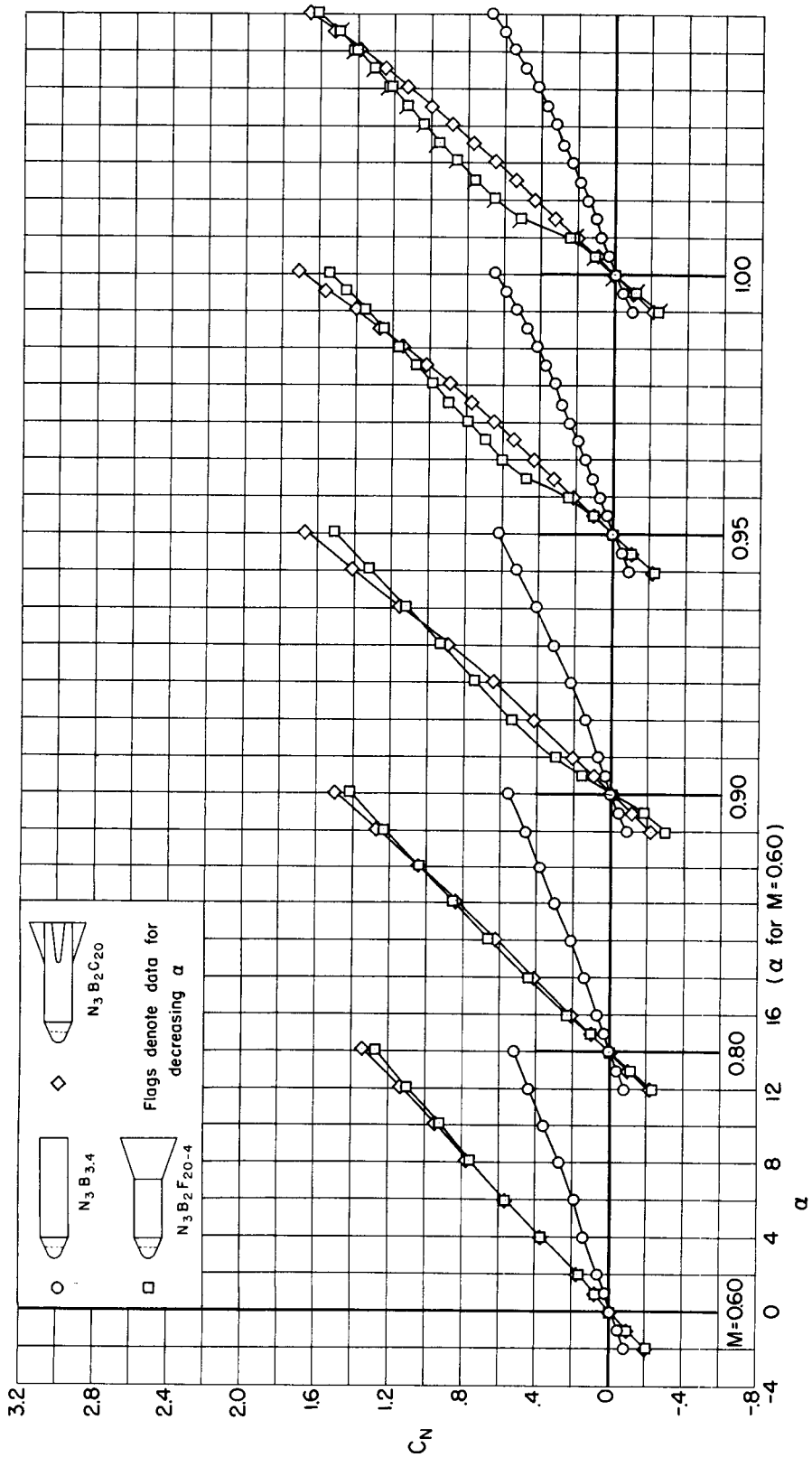
(a) Normal-force coefficient; M = 0.60 to 1.00.

Figure 4.- Static longitudinal aerodynamic coefficients for models with the N_3 nose.
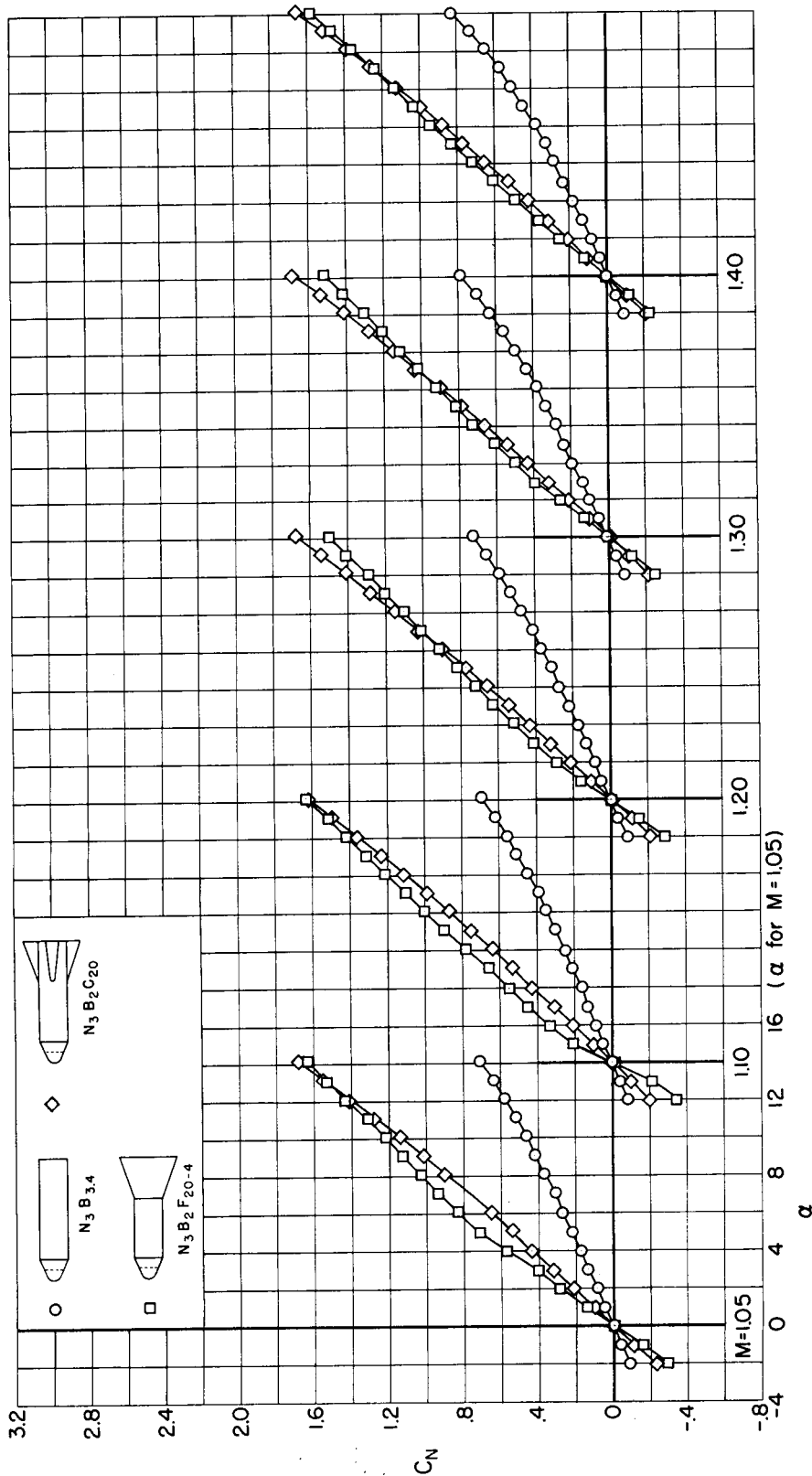
(b) Normal-force coefficient; M = 1.05 to 1.40.

Figure 4.- Continued.

A
4
2
8
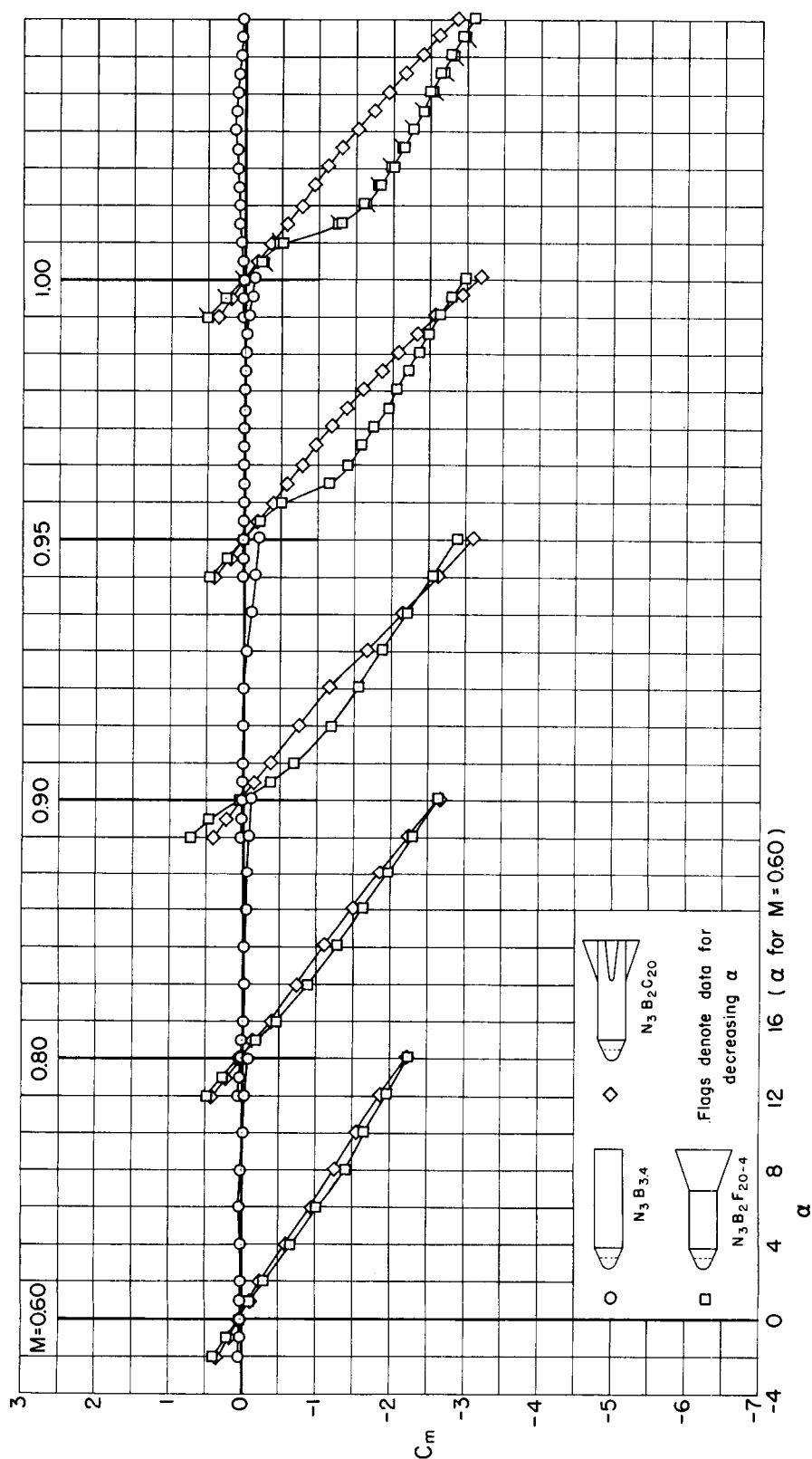
(c) Pitching-moment coefficient; M = 0.60 to 1.00.
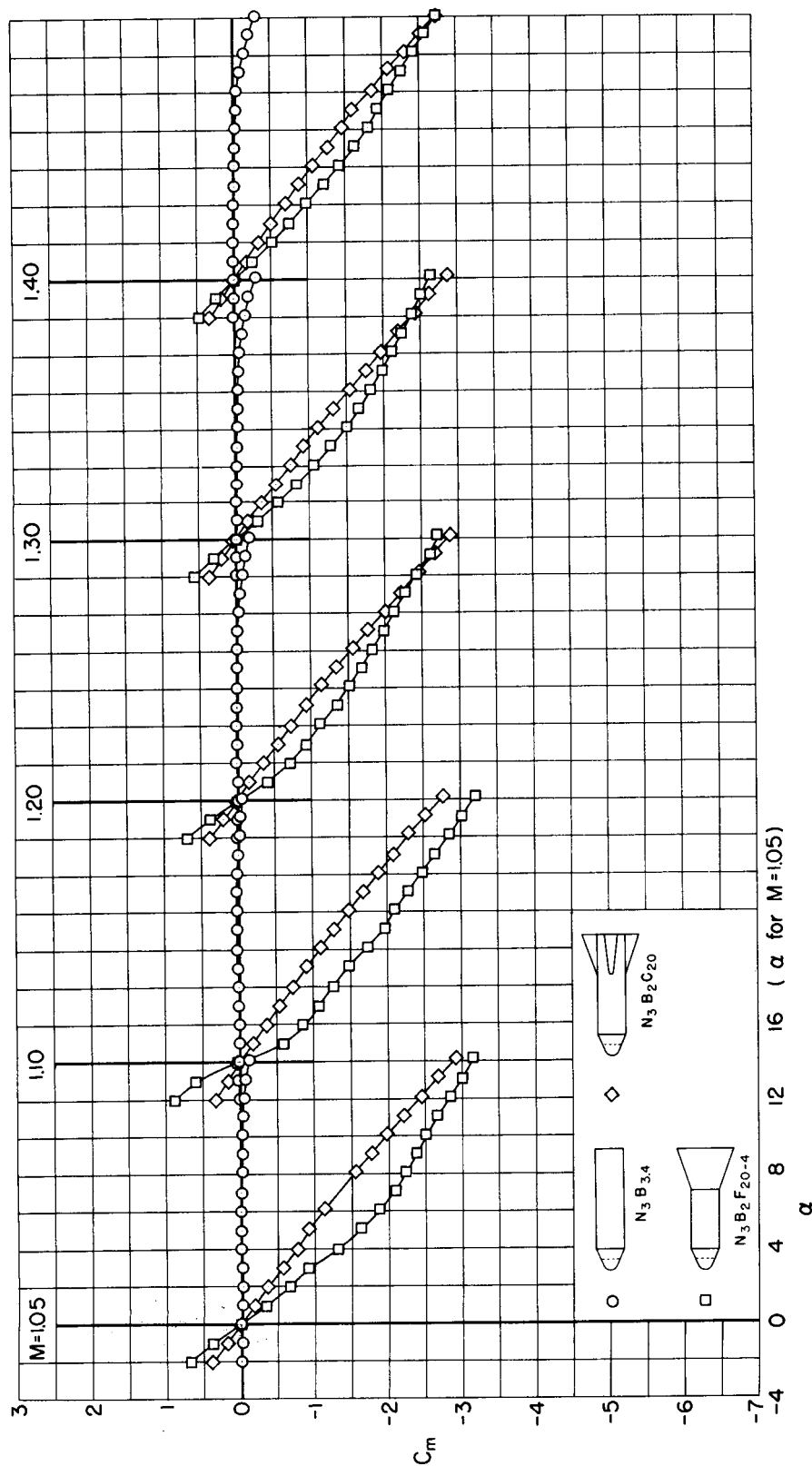
Figure 4.- Continued.

(d) Pitching-moment coefficient; M = 1.05 to 1.40.
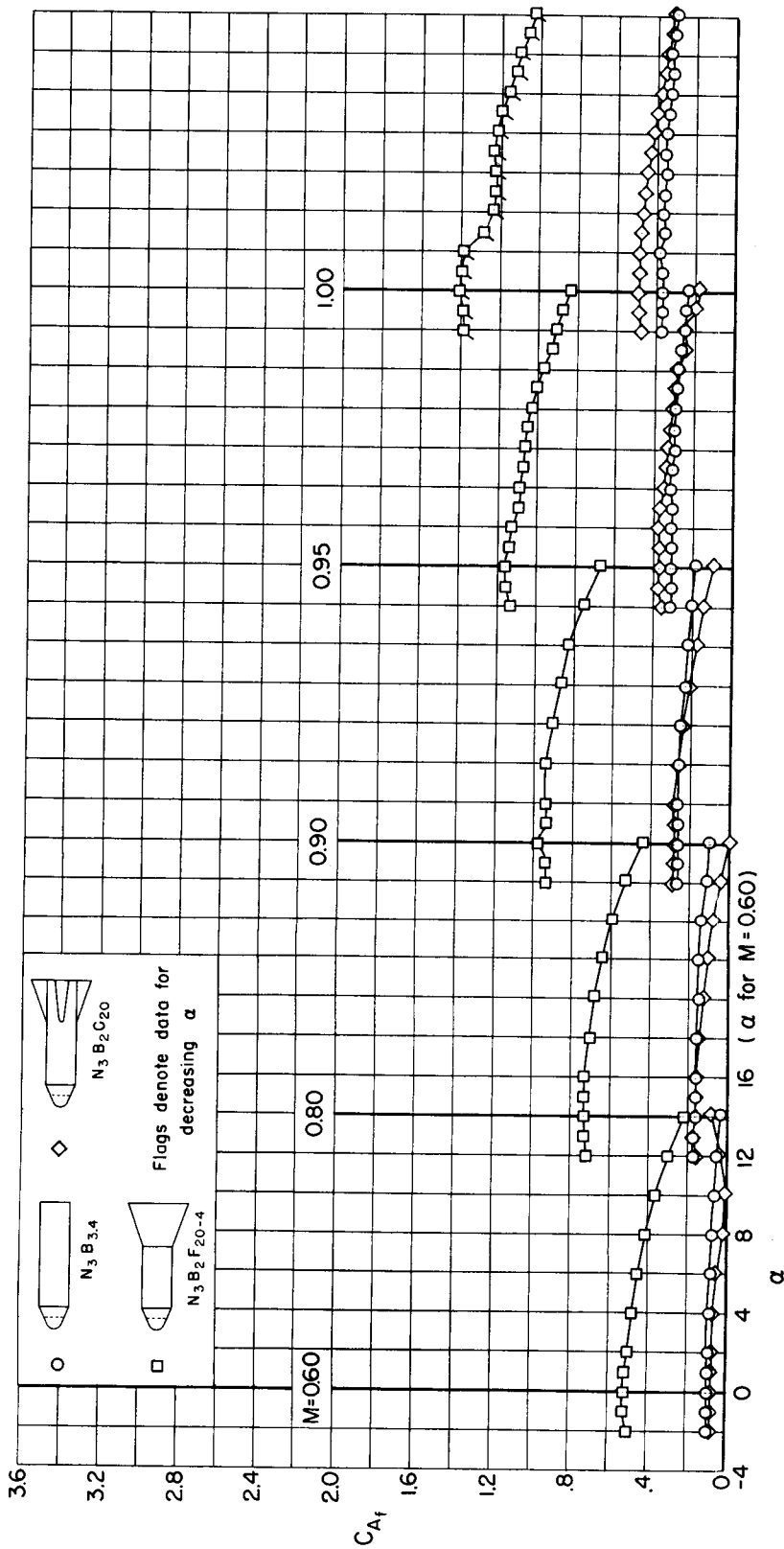
Figure 4.— Continued.

(e) Forebody axial-force coefficient; M = 0.60 to 1.00.
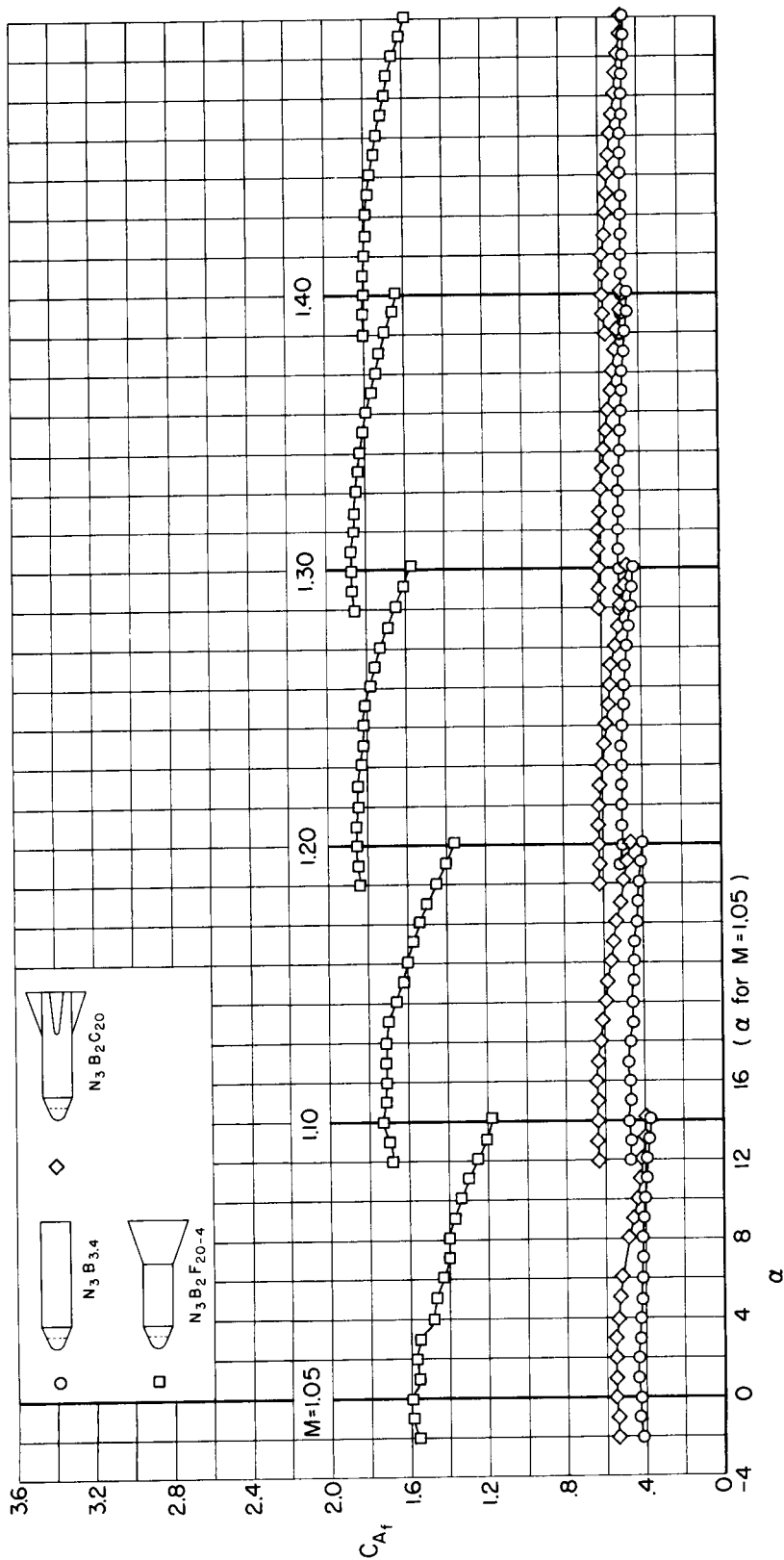
Figure 4.– Continued.

(f) Forebody axial-force coefficient; M = 1.05 to 1.40.

Figure 4.- Continued.

A
428
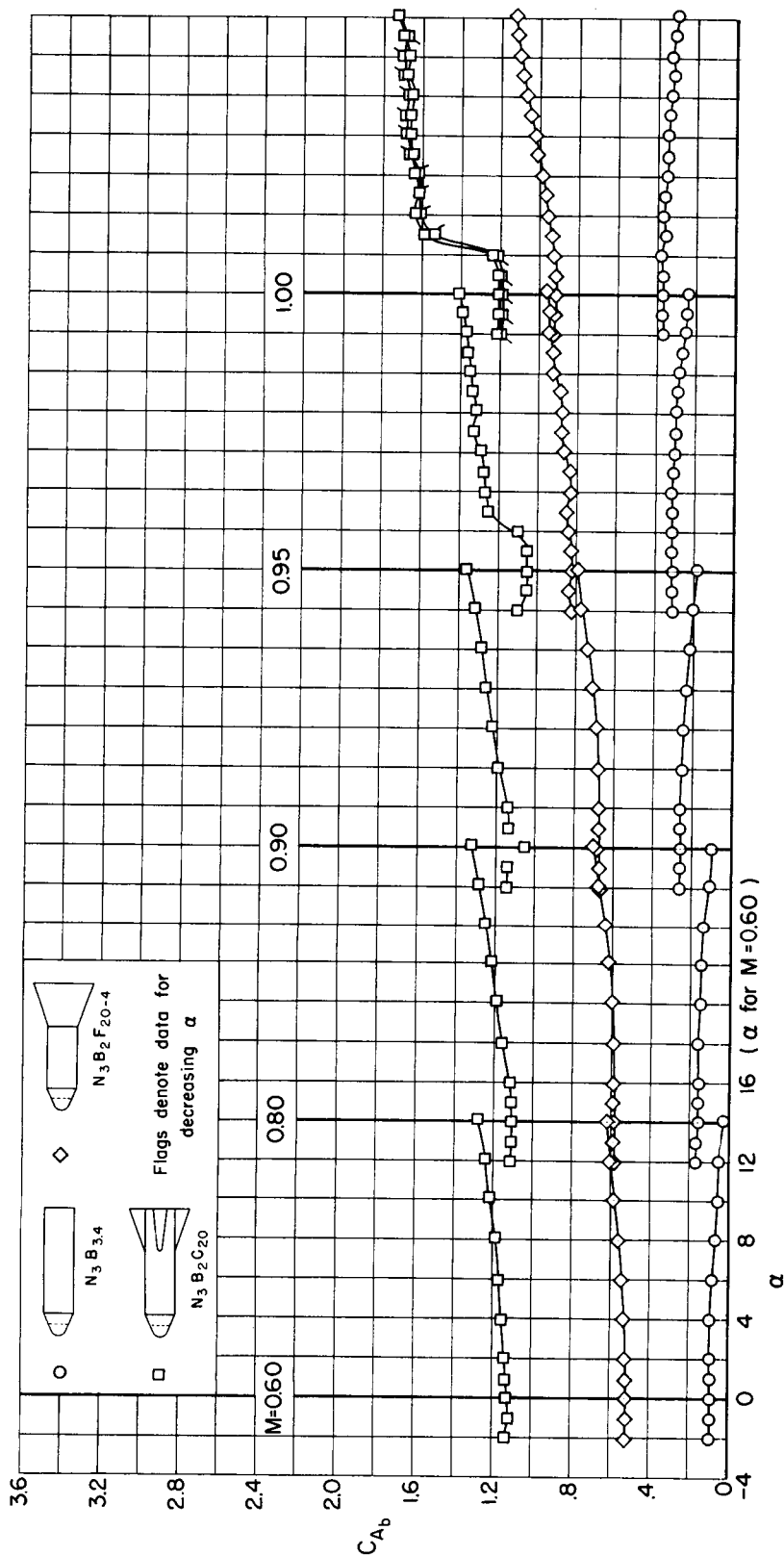
(g) Base axial-force coefficient; M = 0.60 to 1.00.

Figure 4.- Continued.
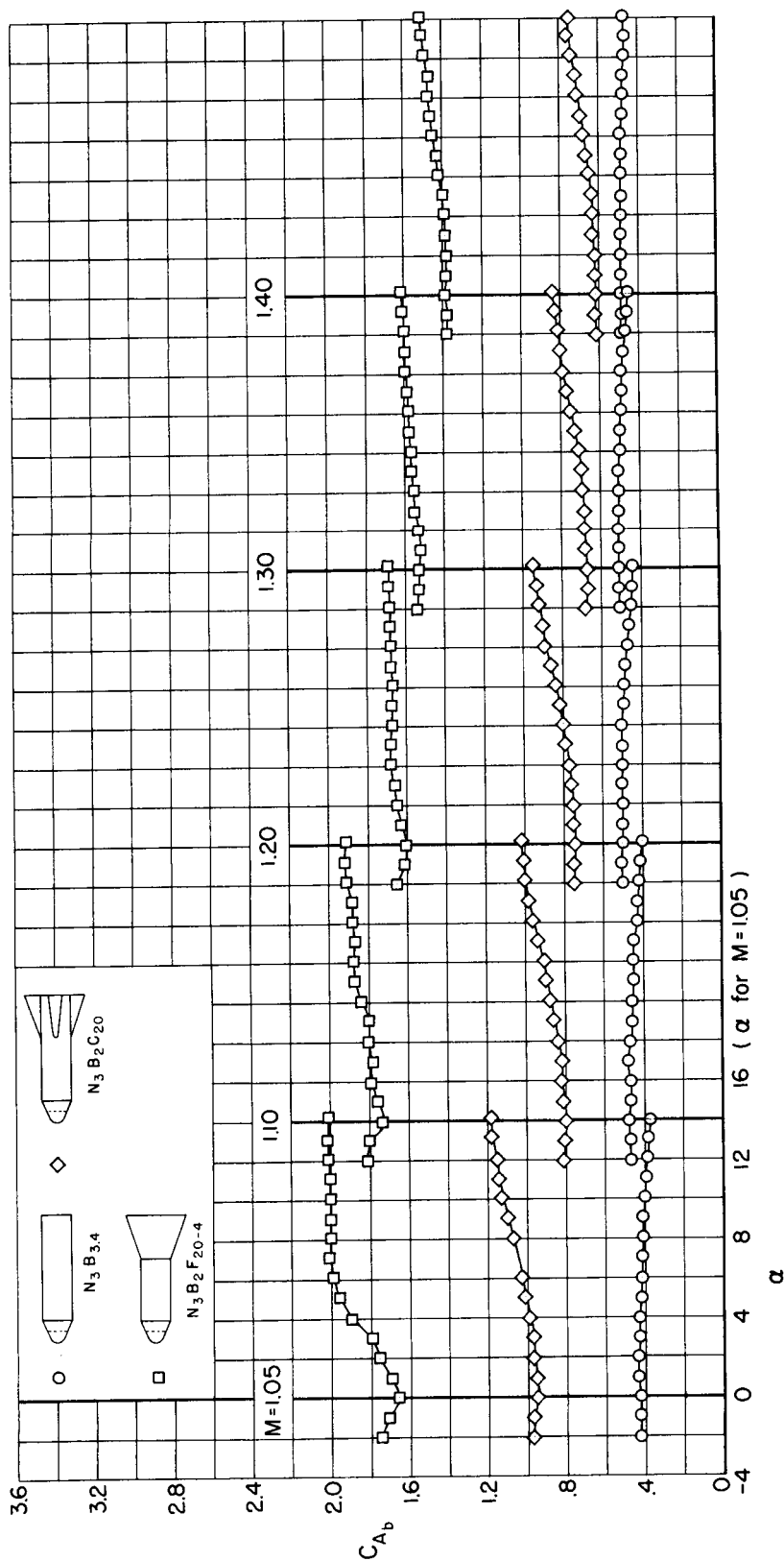
(h) Base axial-force coefficient; M = 1.05 to 1.40.

Figure 4.- Concluded.

A
4
2
8

C_N

3.2 2.8 2.4 2.0 1.6 1.2 .8 .4 0 -.4 -.8

$N_4 B_2 C_{20}$

Flags denote data for decreasing α

$N_4 B_{3,4}$

$N_4 B_2 F_{20-4}$

-4 0 4 8 12 16 (α for M=0.60)

α

M=0.60 0.80 0.90 0.95 1.00
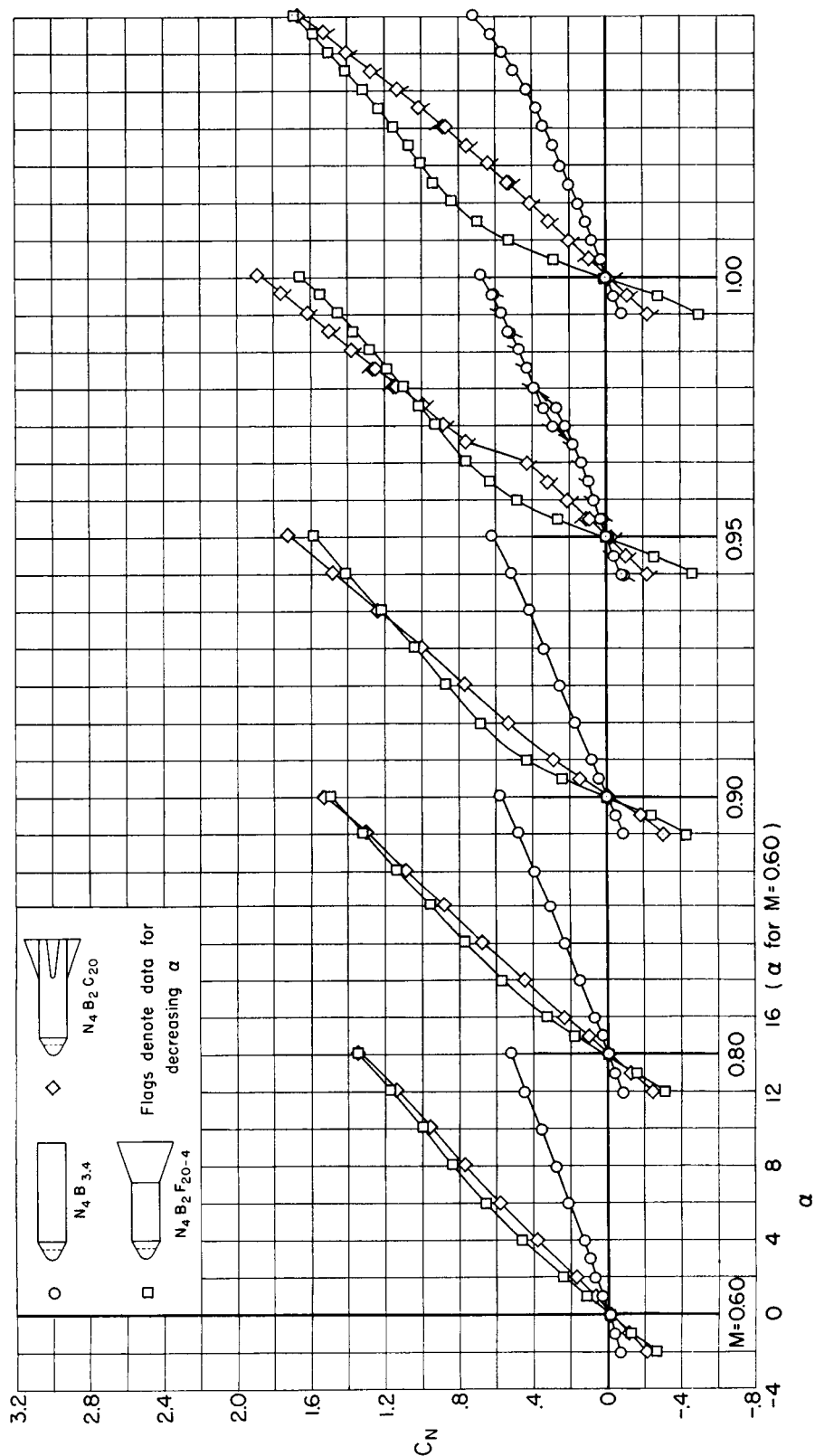
(a) Normal-force coefficient; M = 0.60 to 1.00.

Figure 5.- Static longitudinal aerodynamic coefficients for models with the N_4 nose.
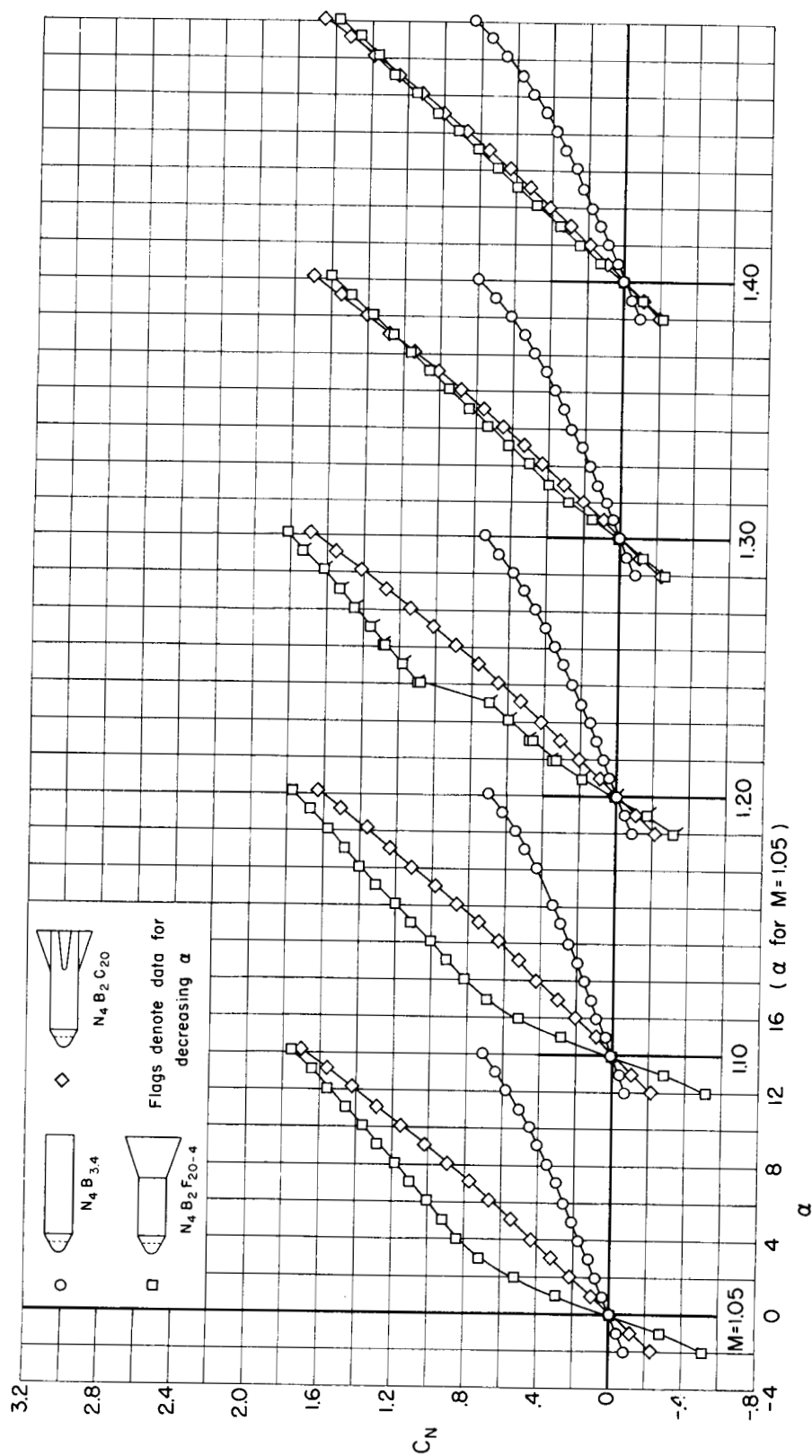
(b) Normal-force coefficient; M = 1.05 to 1.40.
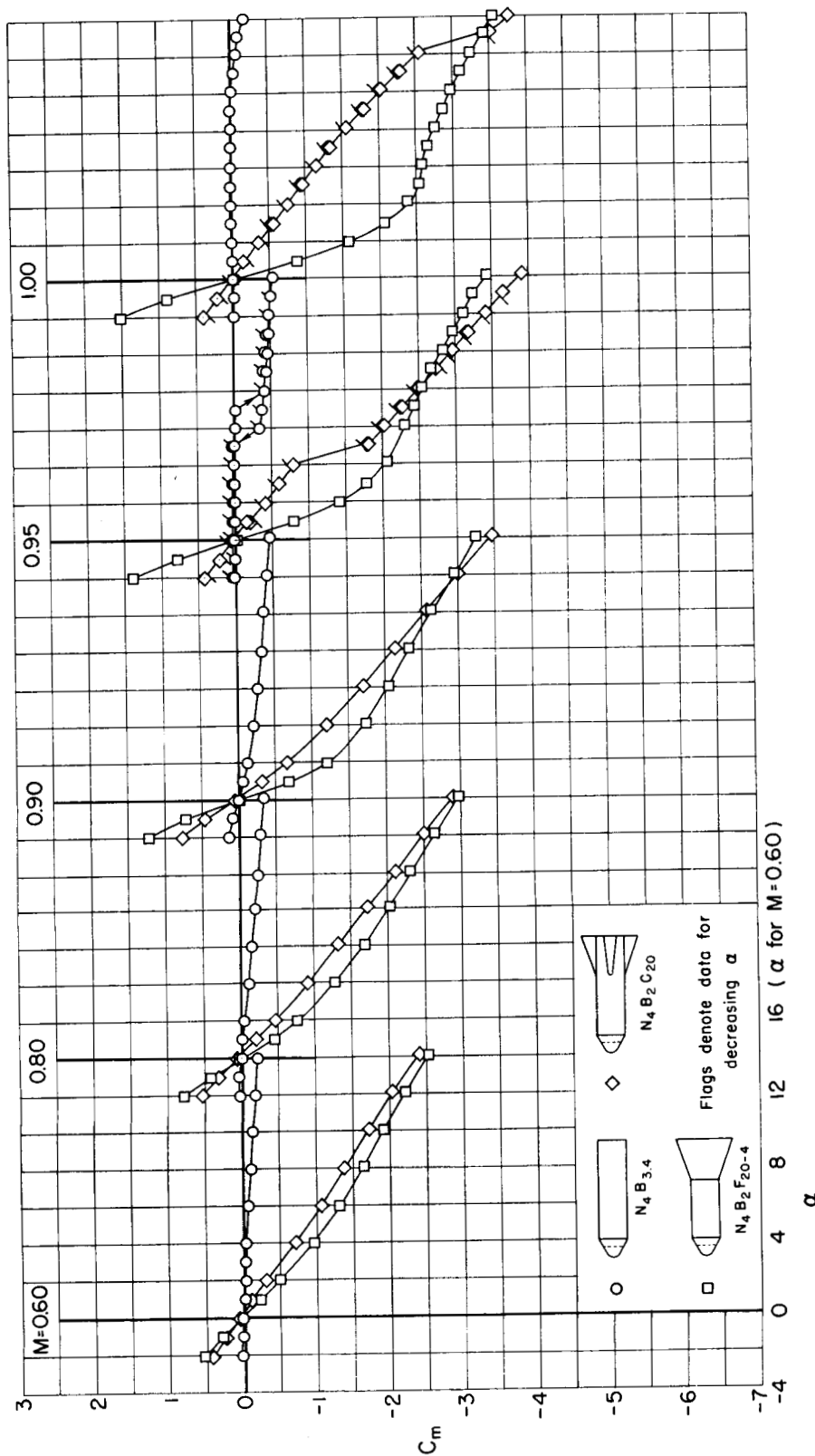
Figure 5.- Continued.

(c) Pitching-moment coefficient; M = 0.60 to 1.00.
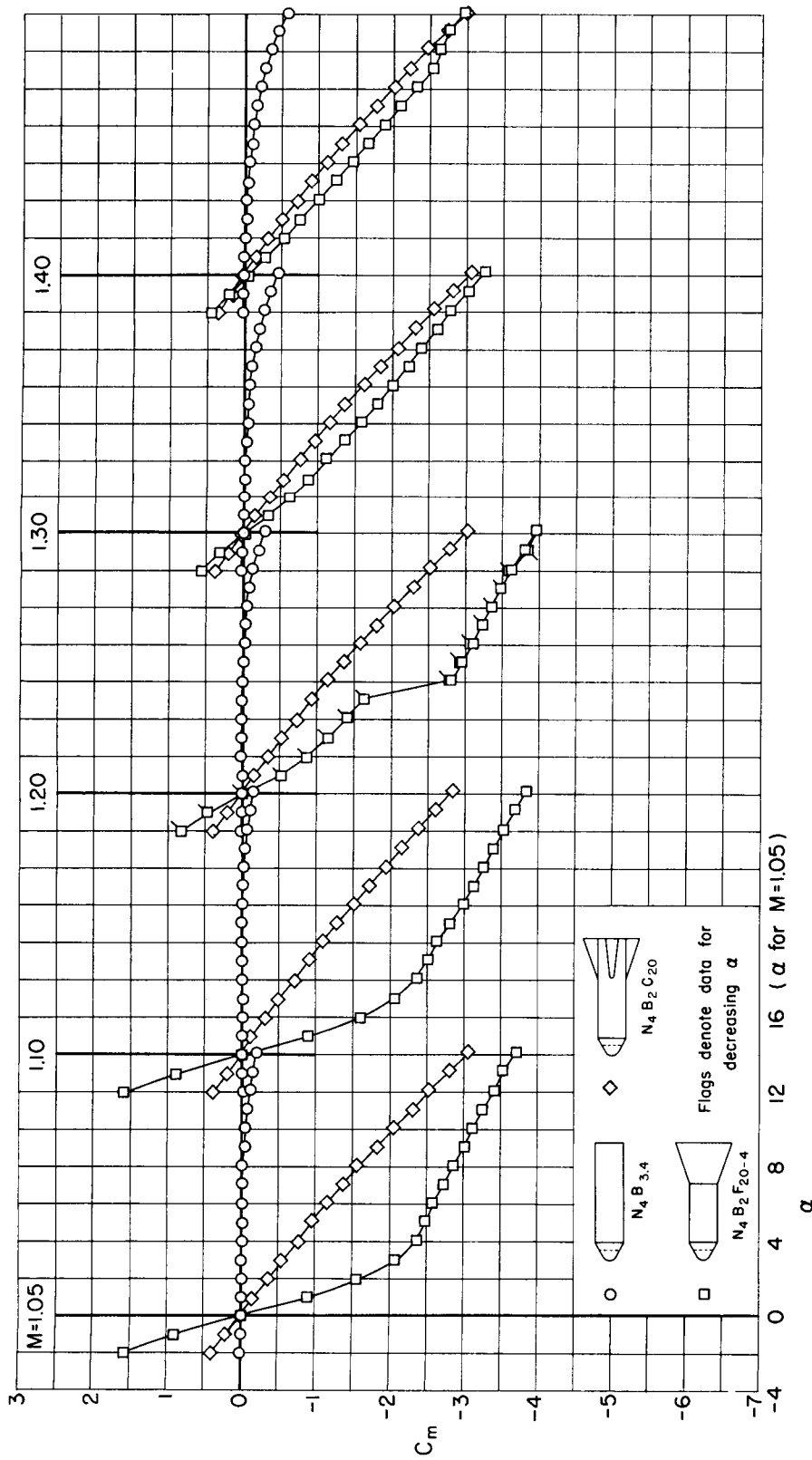
Figure 5.- Continued.

(d) Pitching-moment coefficient; M = 1.05 to 1.40.

Figure 5.- Continued.

A
4
2
8
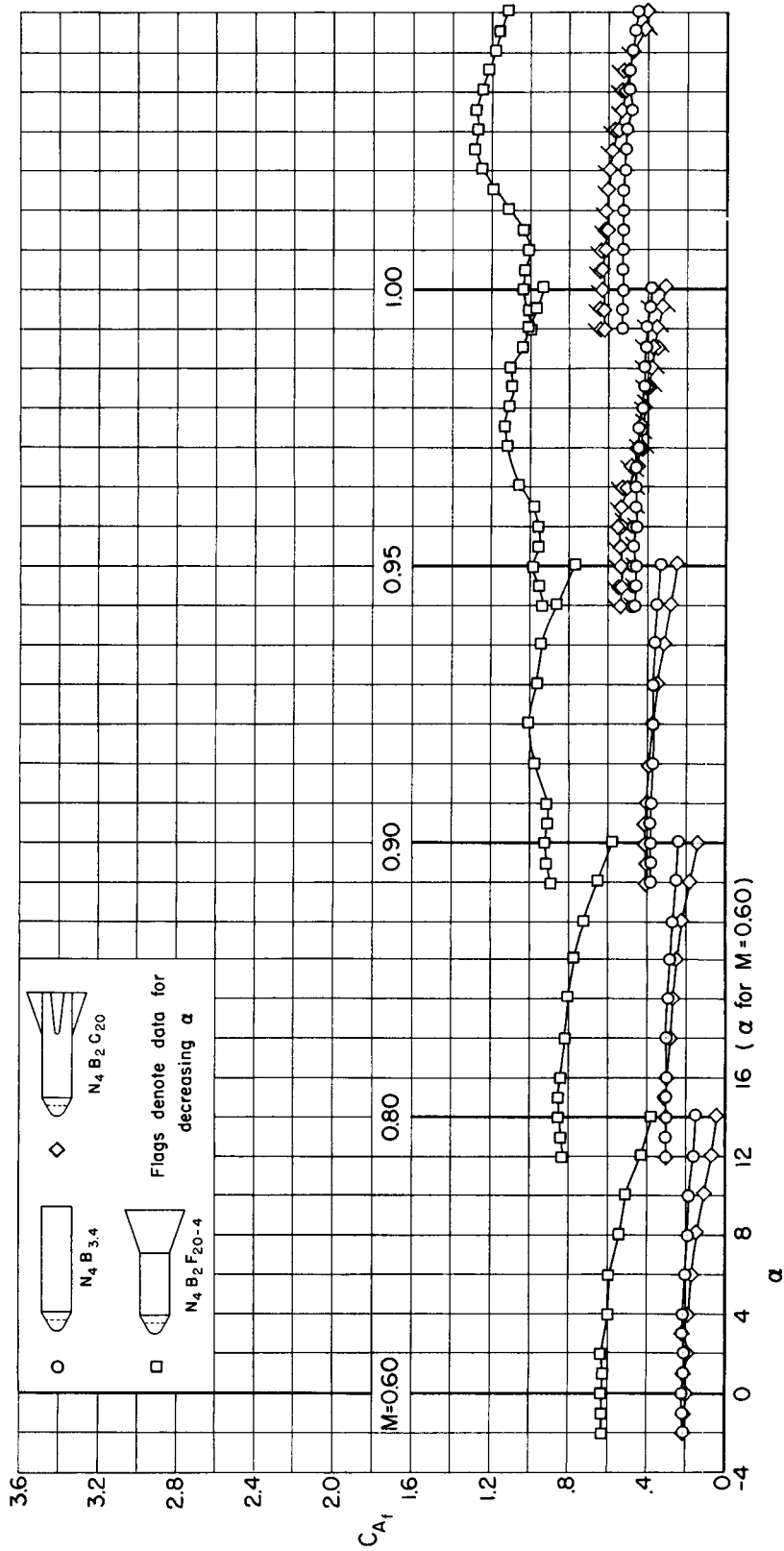
(e) Forebody axial-force coefficient; M = 0.60 to 1.00.

Figure 5.- Continued.

(f) Forebody axial-force coefficient; M = 1.05 to 1.40.

Figure 5.- Continued.

A
4
2
8
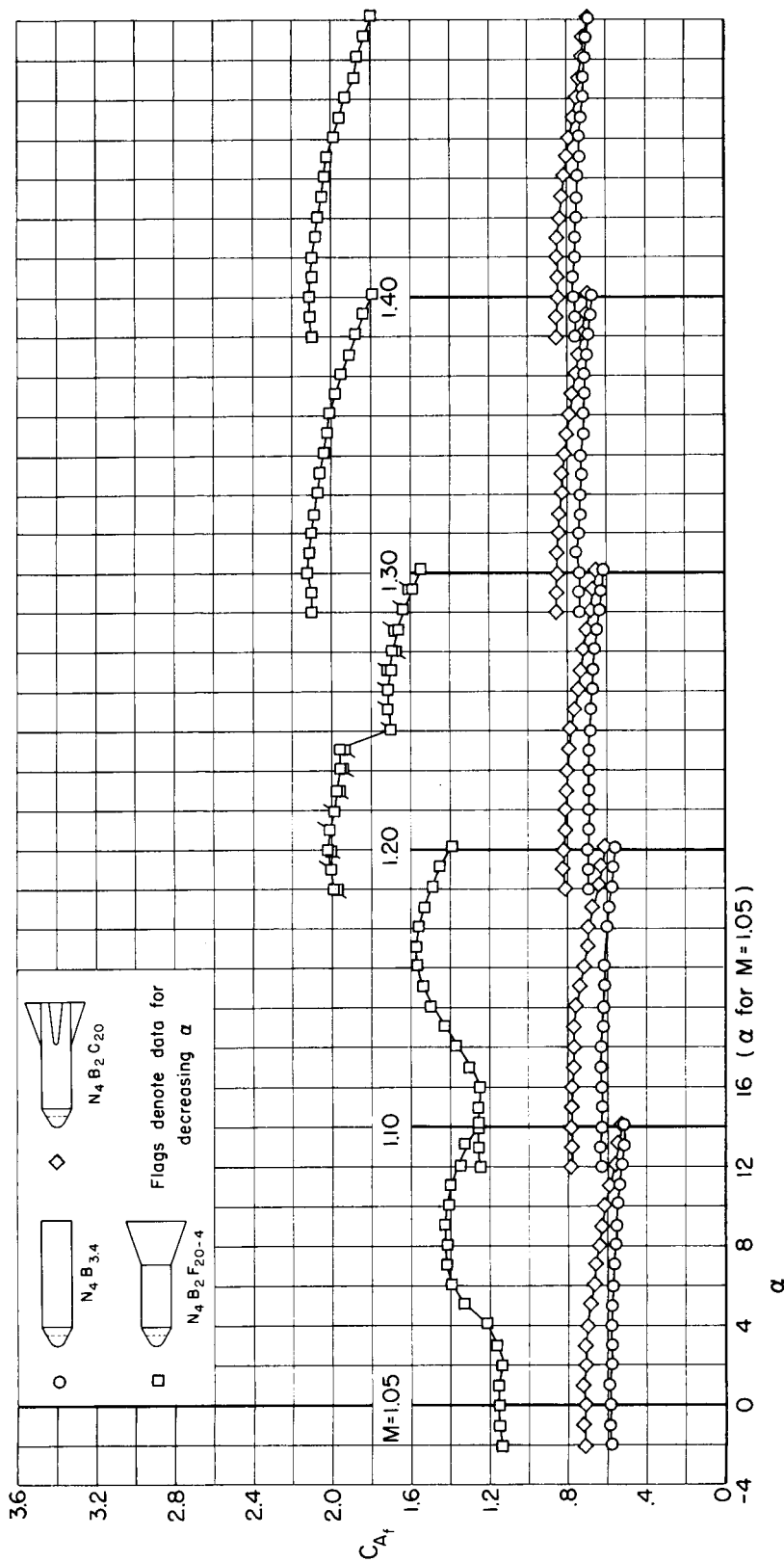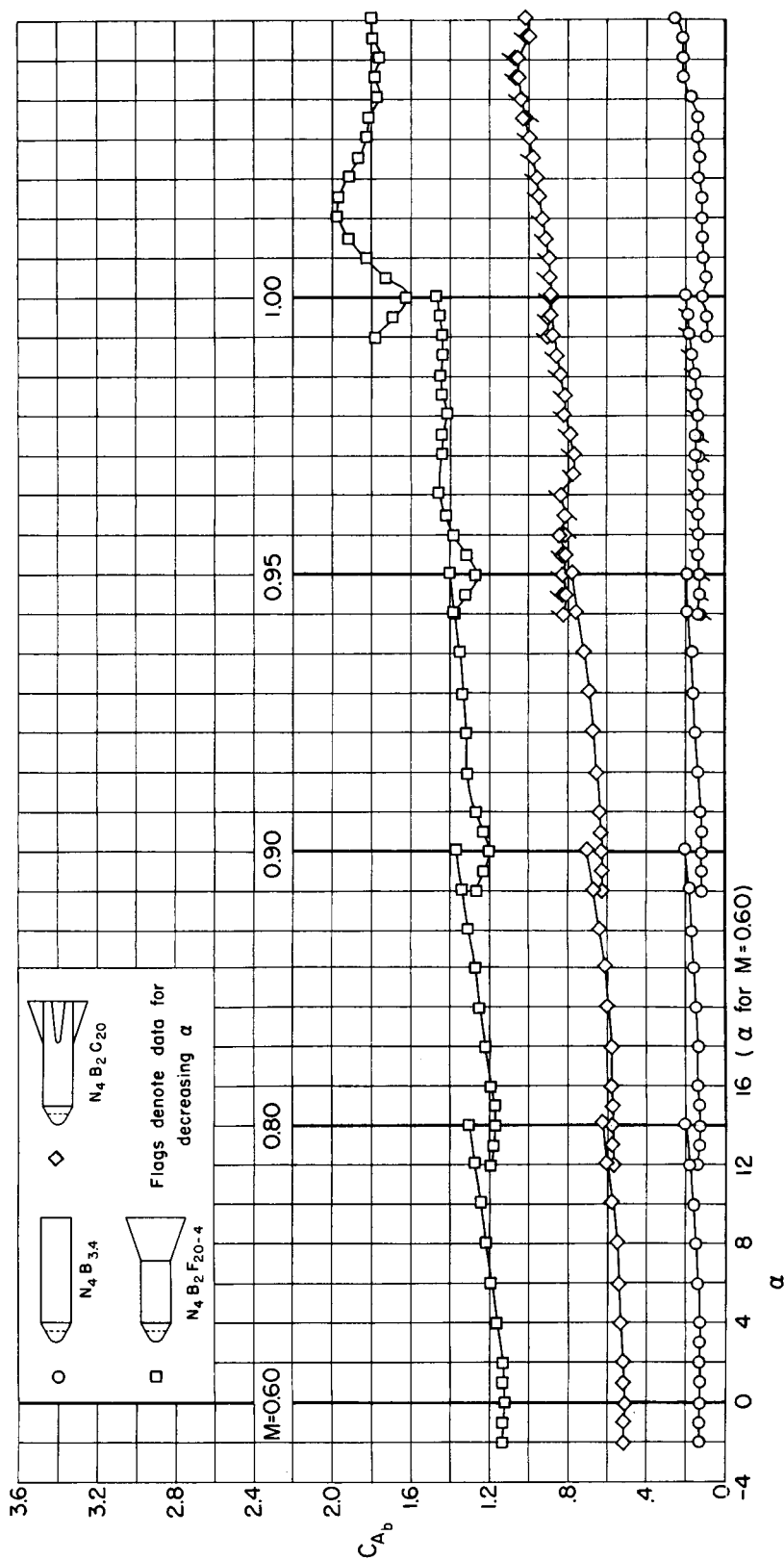
(g) Base axial-force coefficient; M = 0.60 to 1.00.
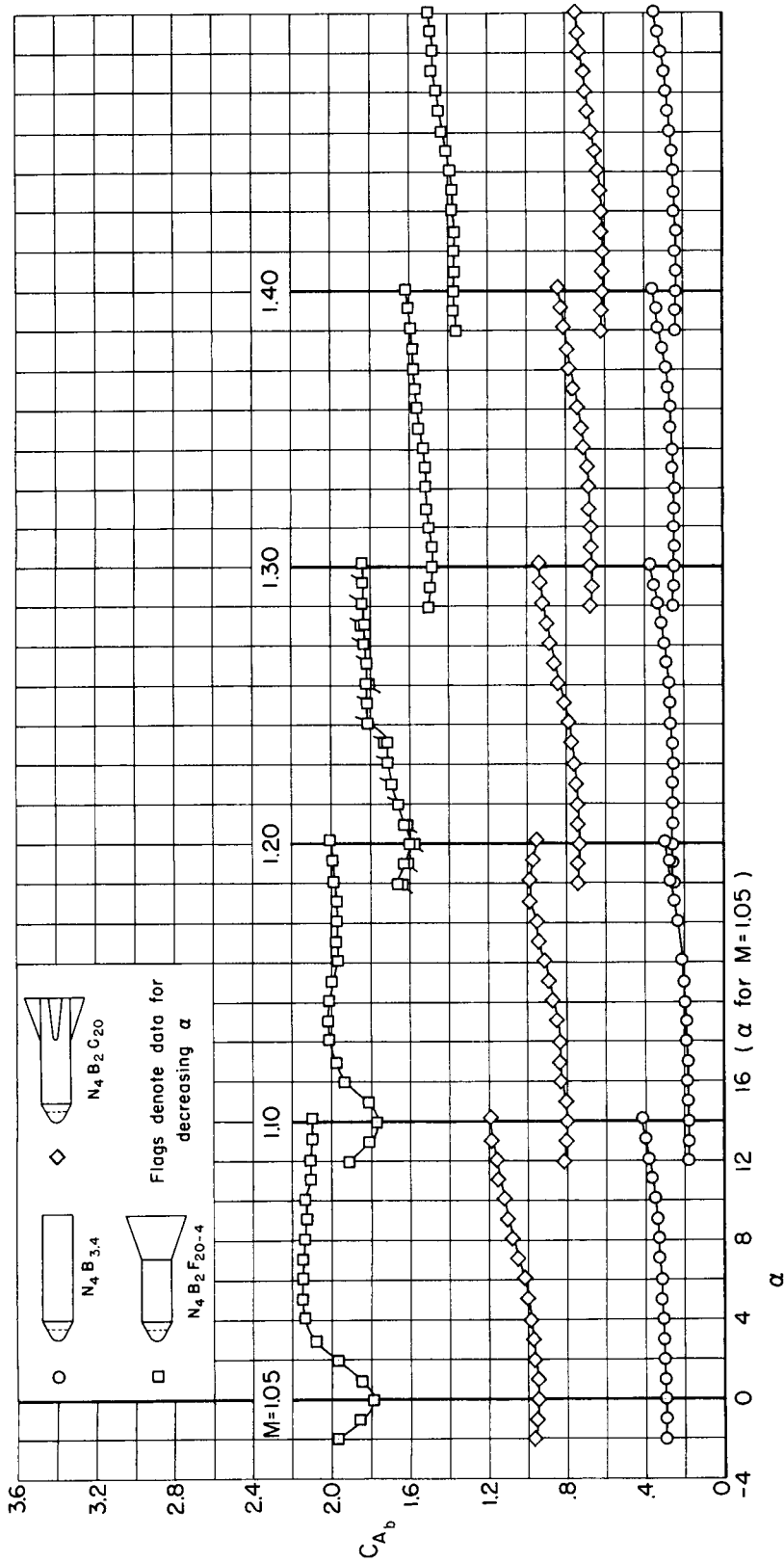
Figure 5.- Continued.

(h) Base axial-force coefficient; M = 1.05 to 1.40.

Figure 5.- Concluded.

A
4
2
8
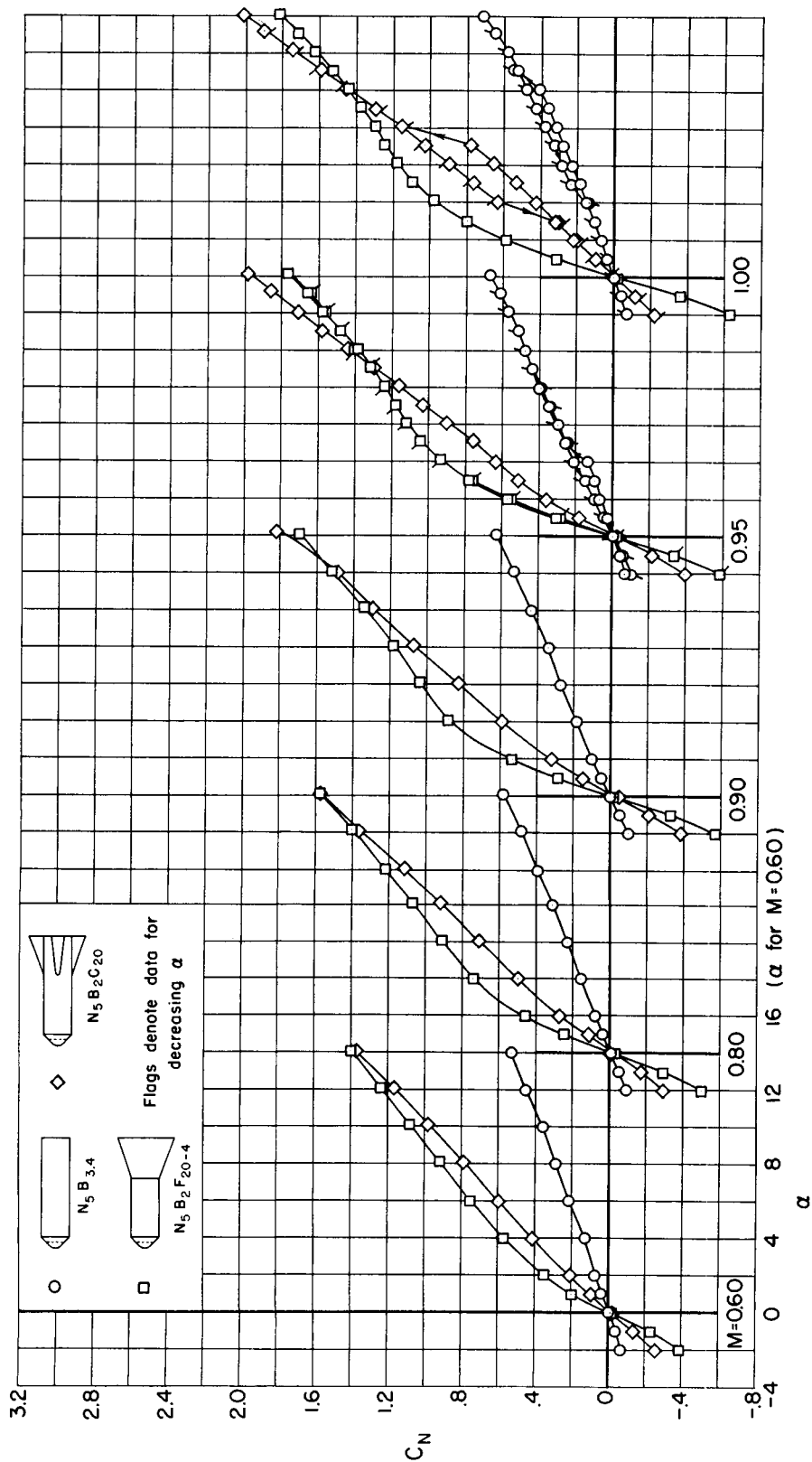
(a) Normal-force coefficient; M = 0.60 to 1.00.

Figure 6.- Static longitudinal aerodynamic coefficients for models with the N_5 nose.
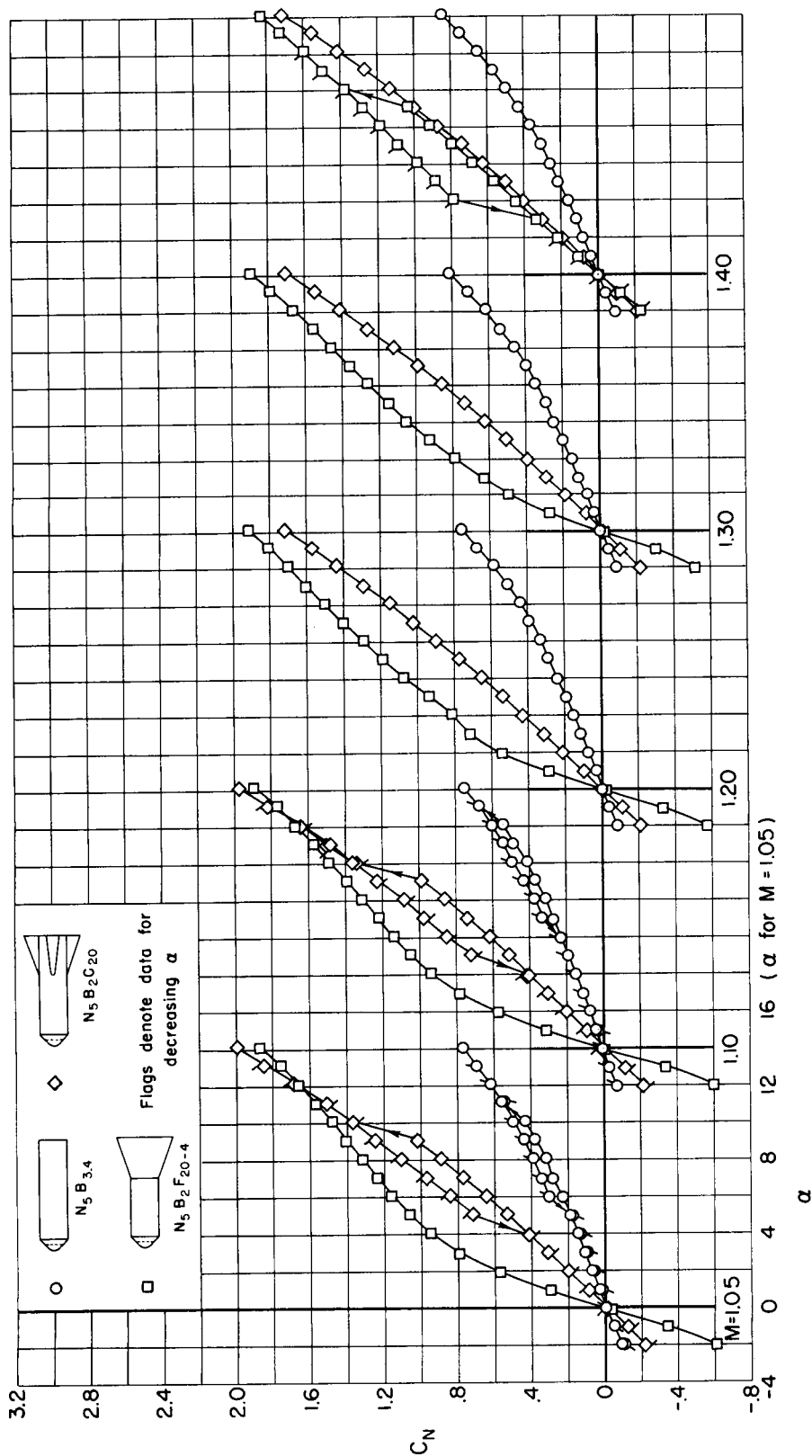
(b) Normal-force coefficient; M = 1.05 to 1.40.
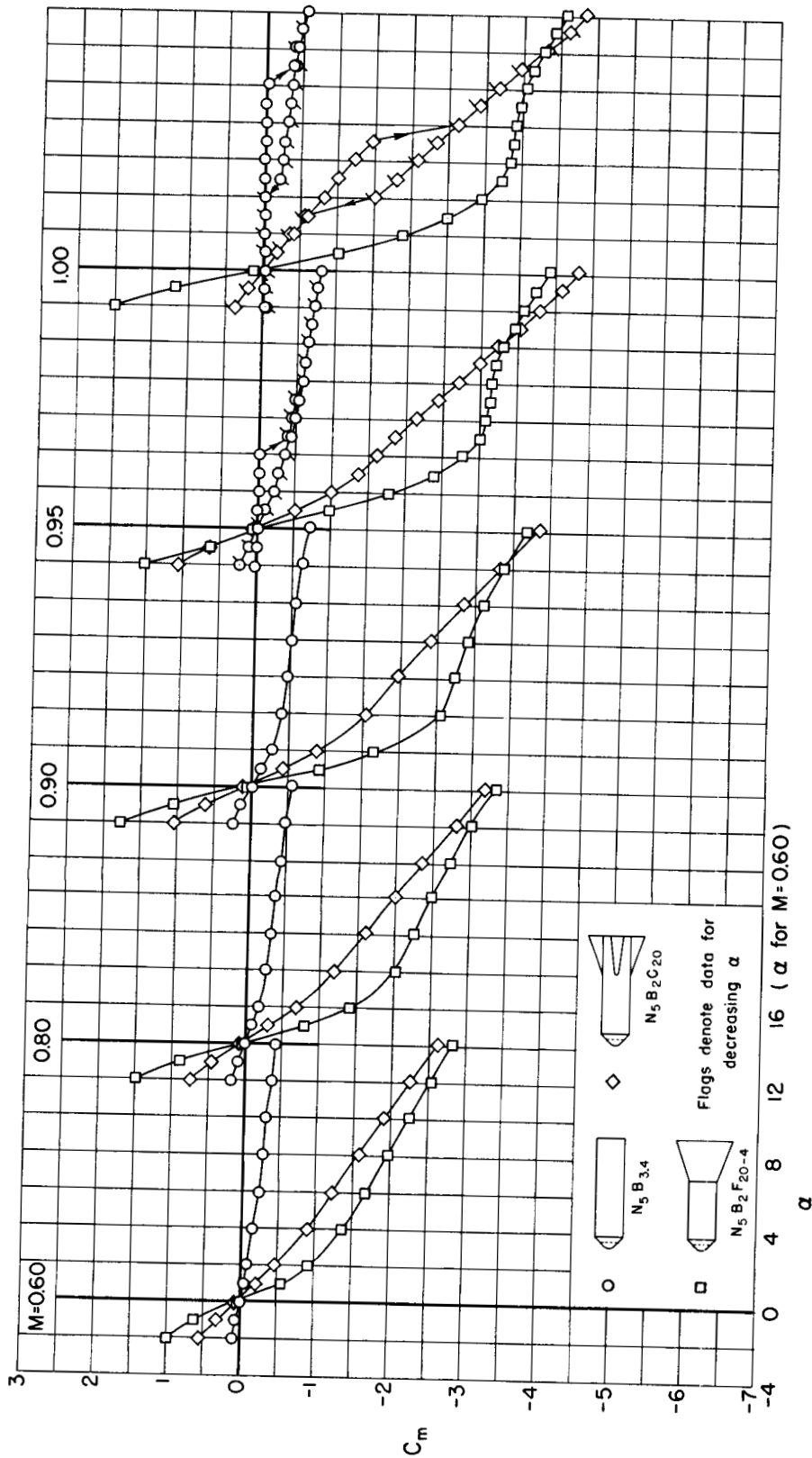
Figure 6.- Continued.

(c) Pitching-moment coefficient; M = 0.60 to 1.00.

Figure 6.- Continued.

36
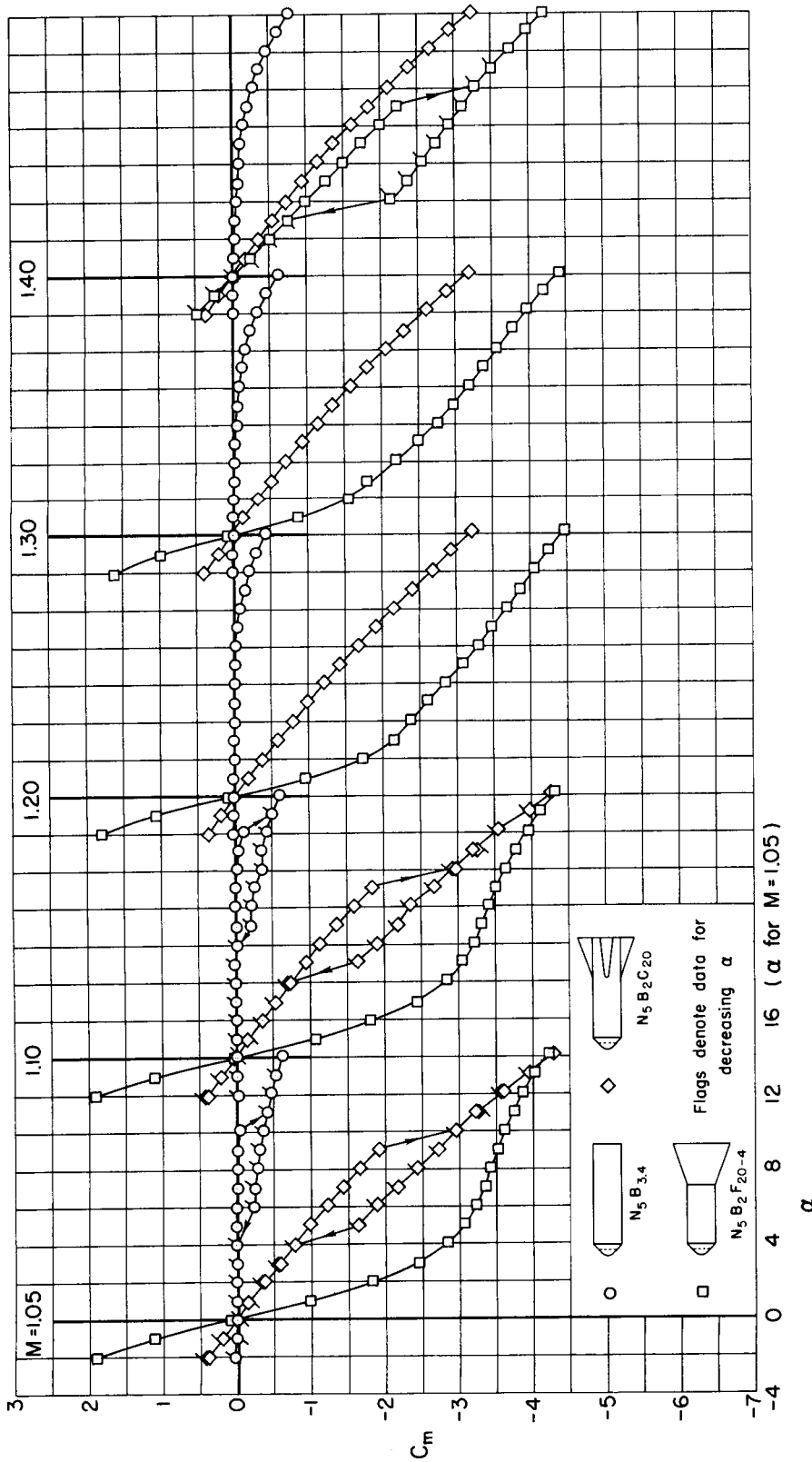
(d) Pitching-moment coefficient; M = 1.05 to 1.40.
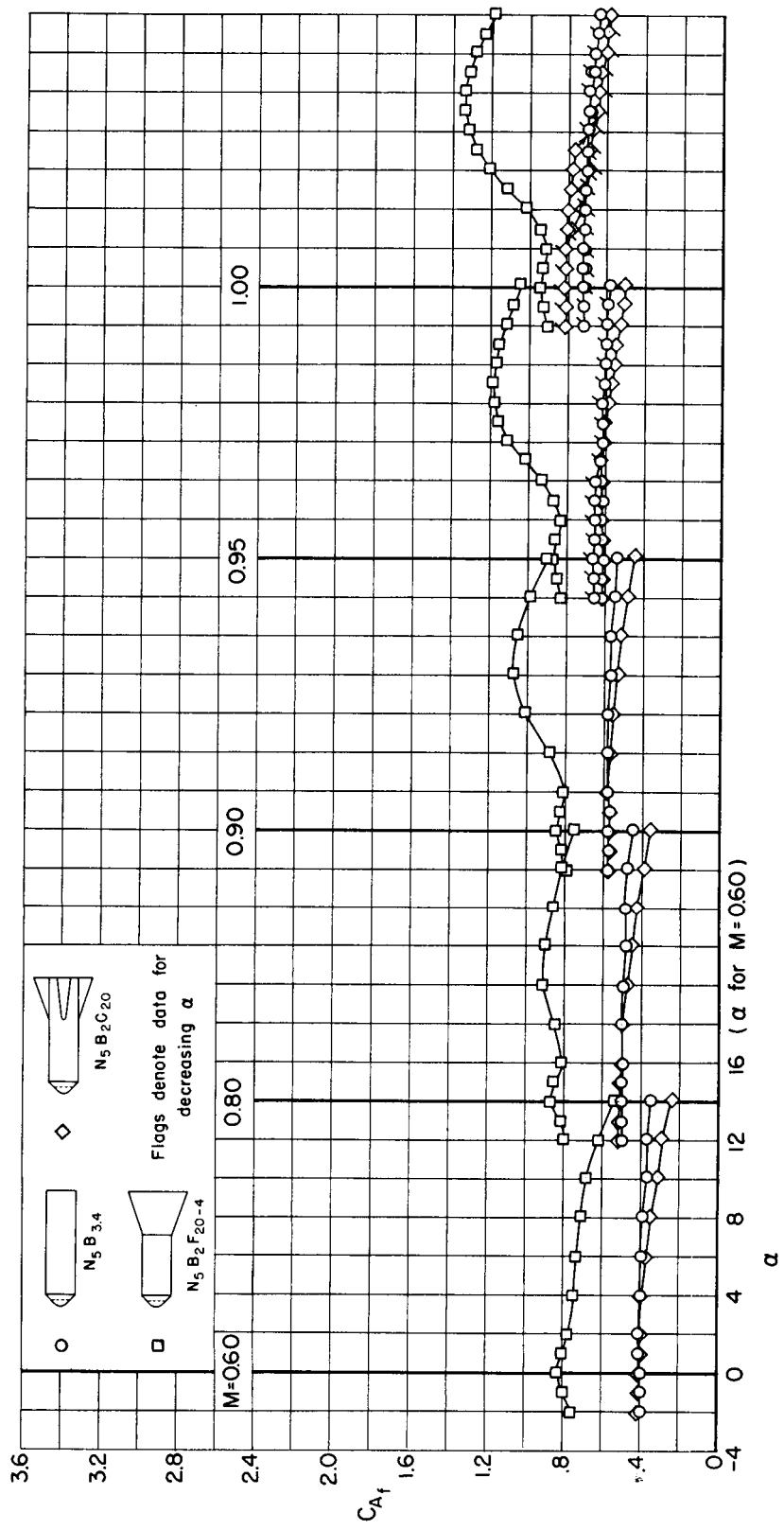
Figure 6.- Continued.

(e) Forebody axial-force coefficient; M = 0.60 to 1.00.
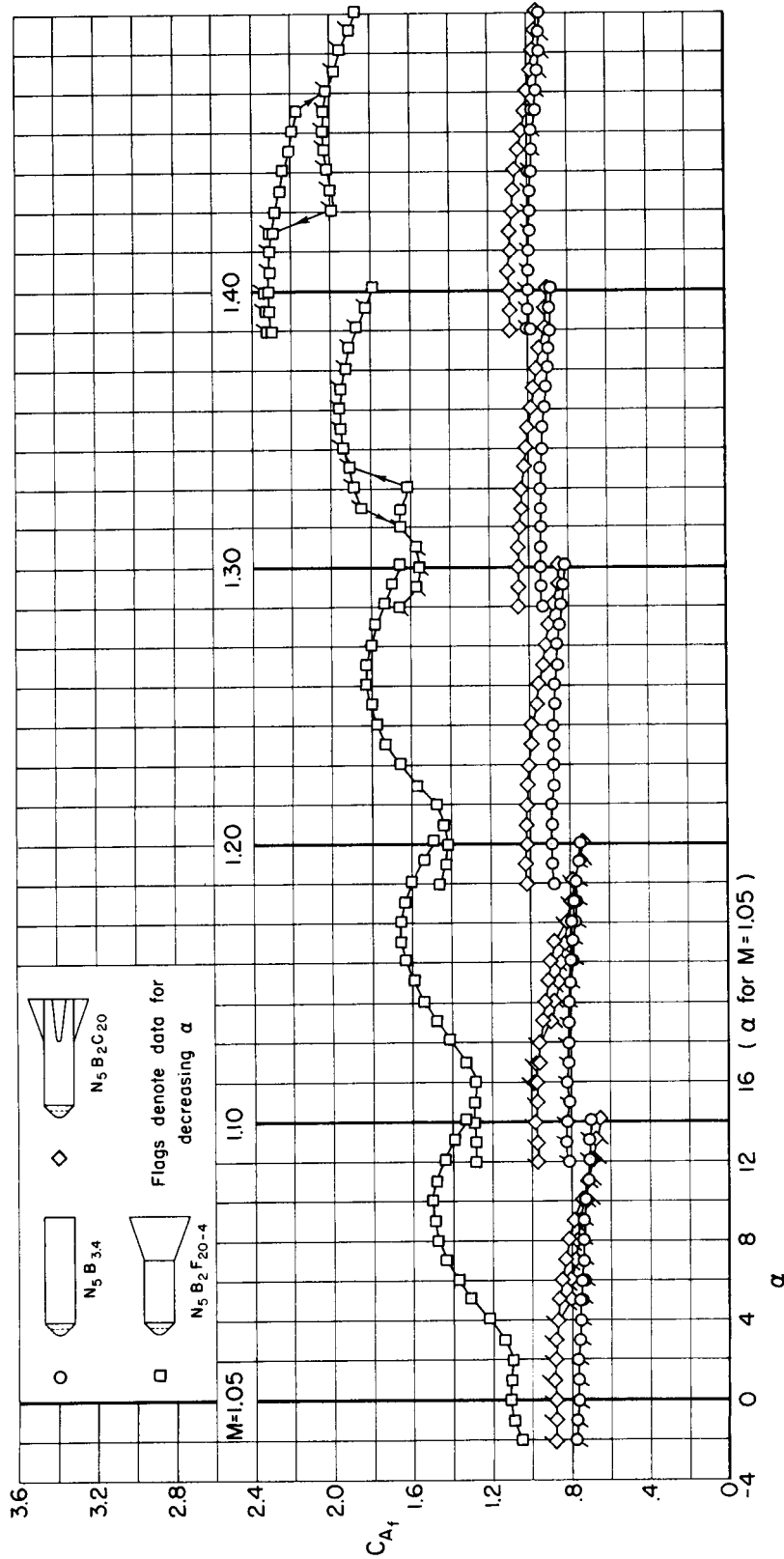
Figure 6.- Continued.

(f) Forebody axial-force coefficient; M = 1.05 to 1.40.
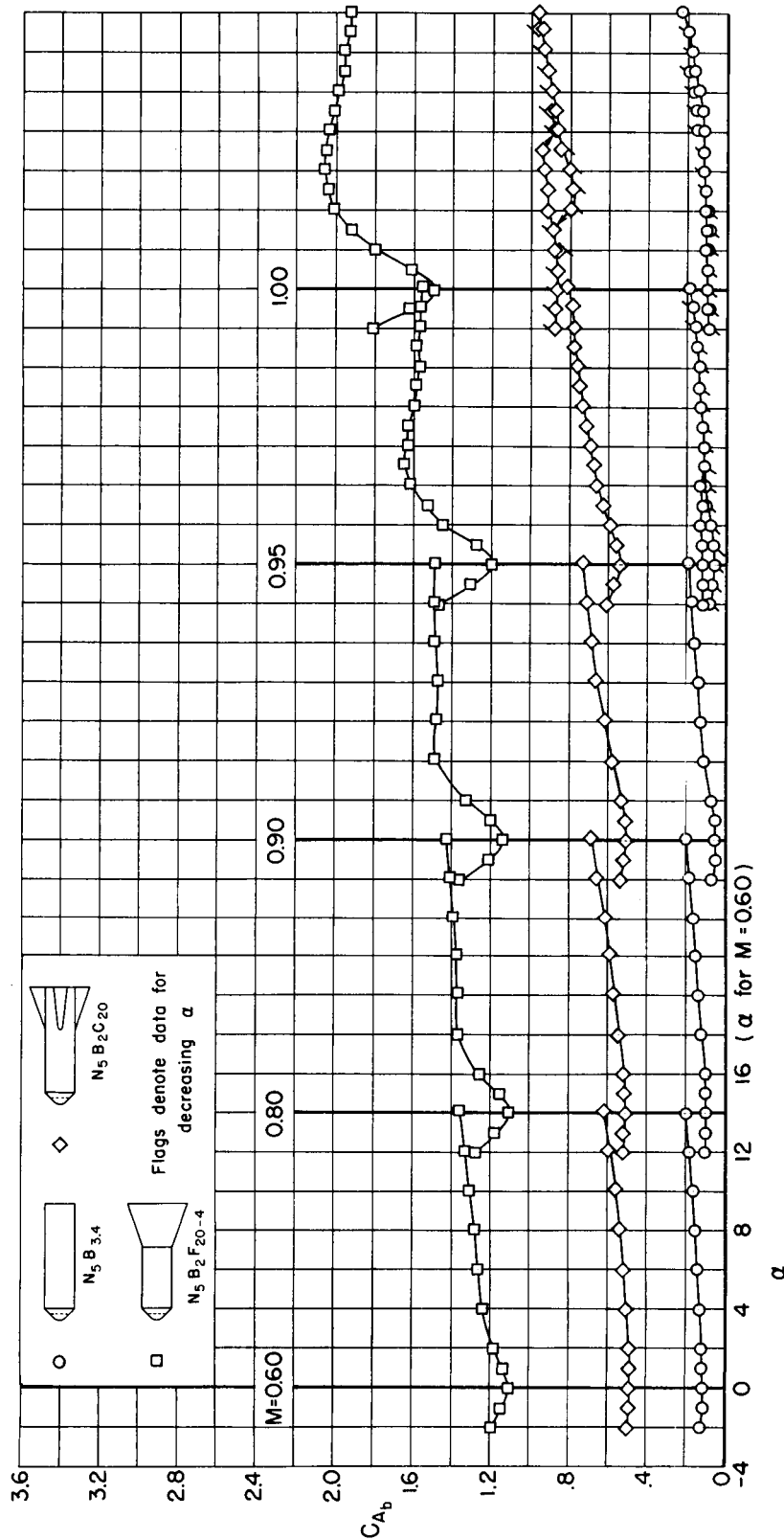
Figure 6.- Continued.

(g) Base axial-force coefficient; M = 0.60 to 1.00.

Figure 6.- Continued.

(h) Base axial-force coefficient; M = 1.05 to 1.40.
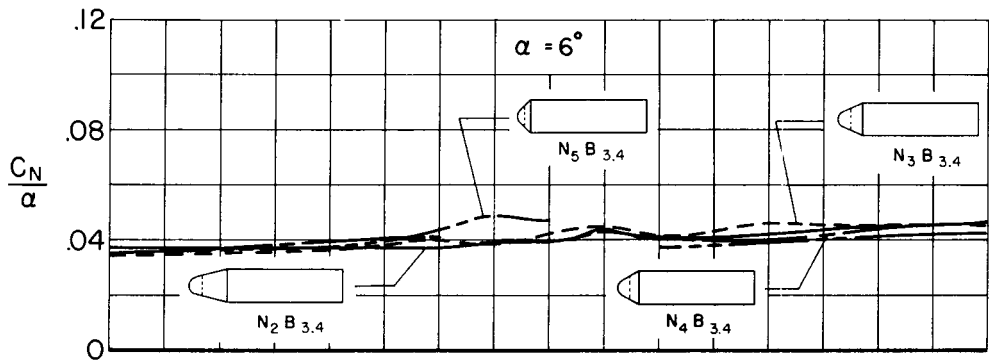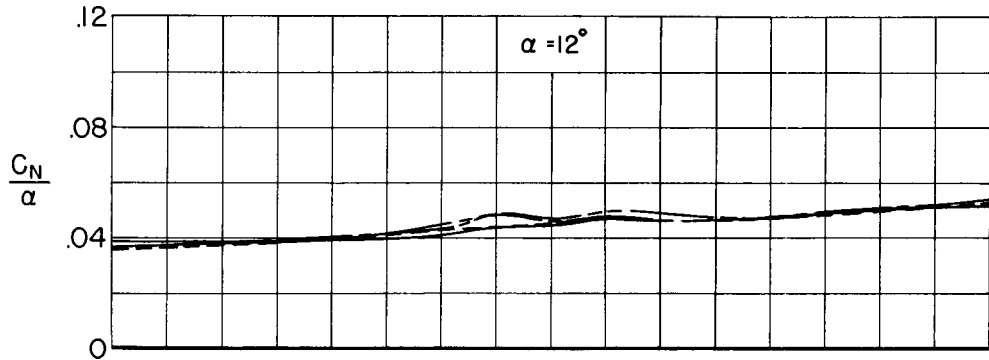
Figure 6.- Continued.

(a) Cylindrical-body models.

Figure 7.- Effects of nose cone angle on the normal-force parameter.

Note: Curves have been deleted where flow hysteresis caused significant differences for increasing and decreasing α
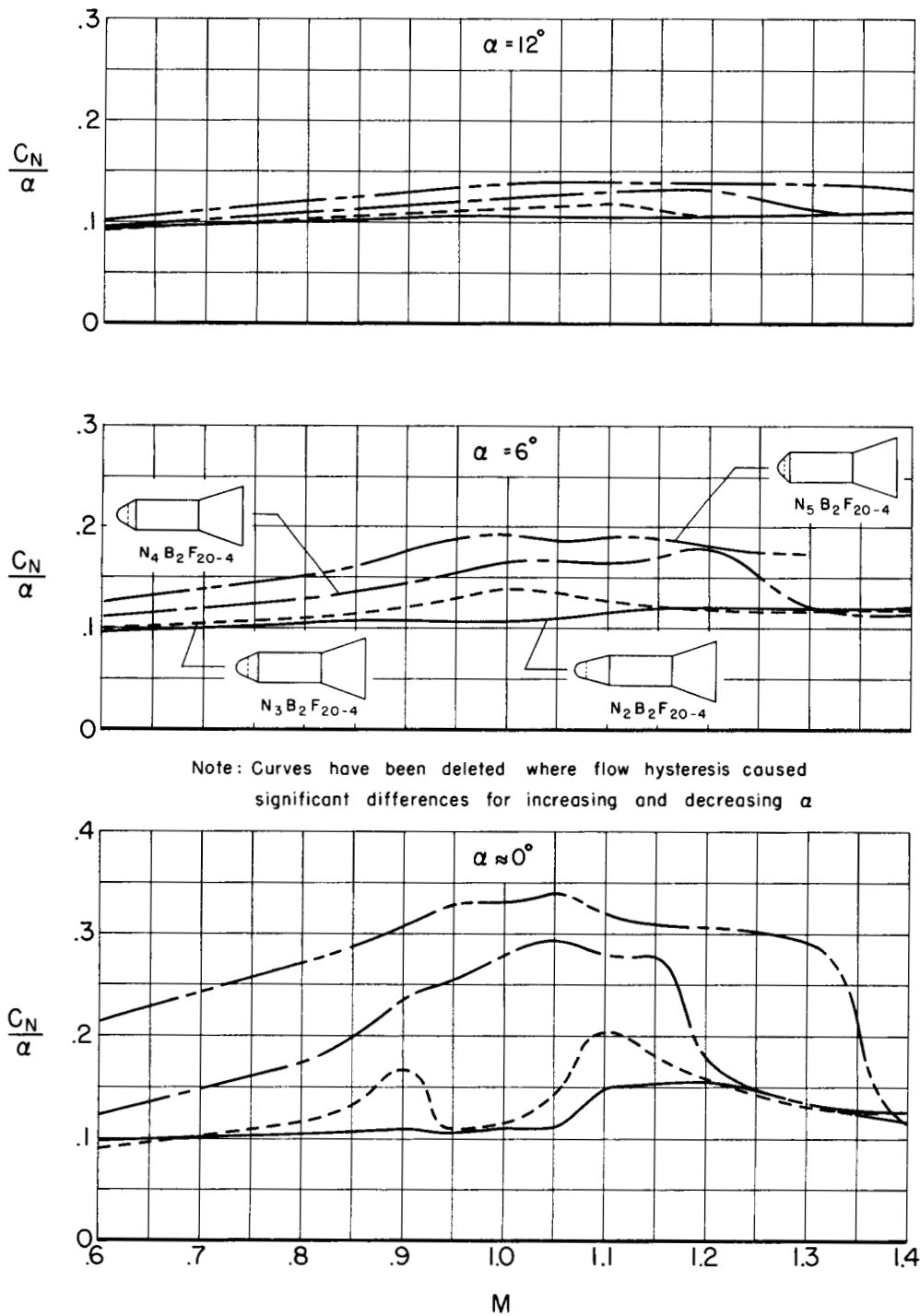
(b) Flared afterbody models.

Figure 7.- Continued.
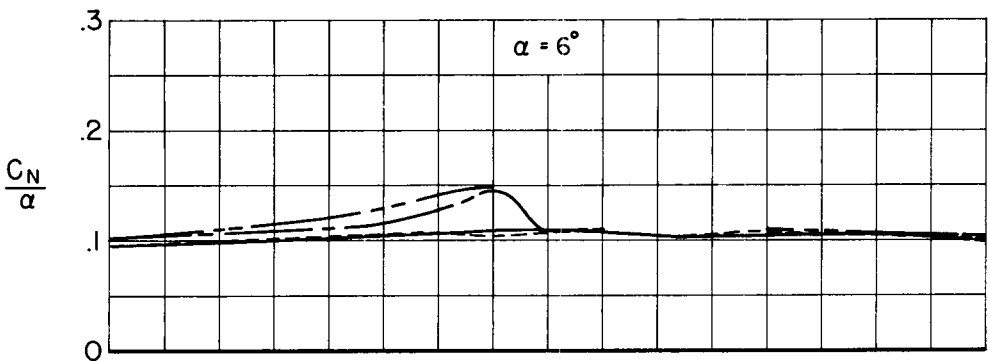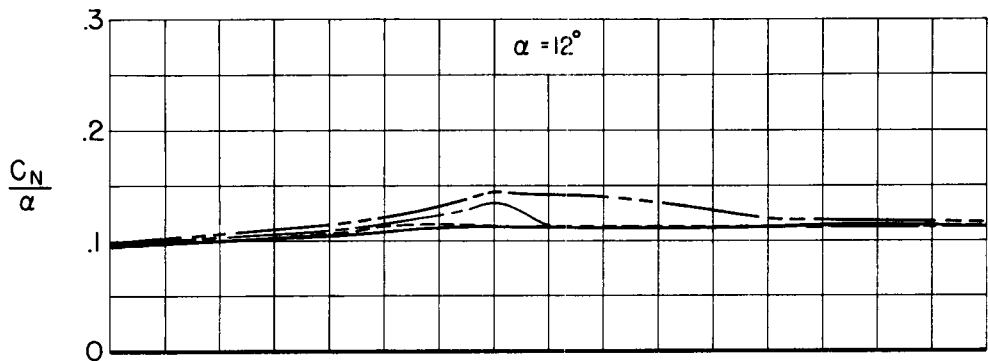
(c) Blunt-finned afterbody models.

Figure 7.- Concluded.
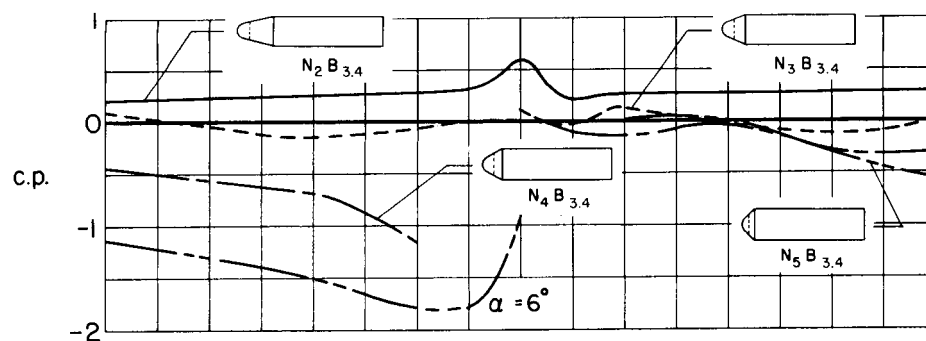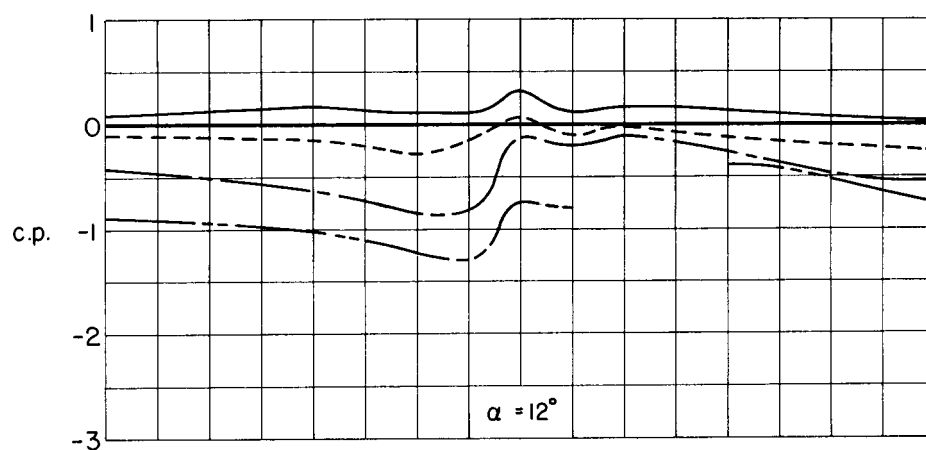
$\alpha = 12°$

c.p.

$N_2 B_{3.4}$ $N_3 B_{3.4}$

$N_4 B_{3.4}$

$N_5 B_{3.4}$

c.p.

$\alpha = 6°$

Note: Curves have been deleted where flow hysteresis caused significant differences for increasing and decreasing α

c.p.

$\alpha \approx 0°$

M
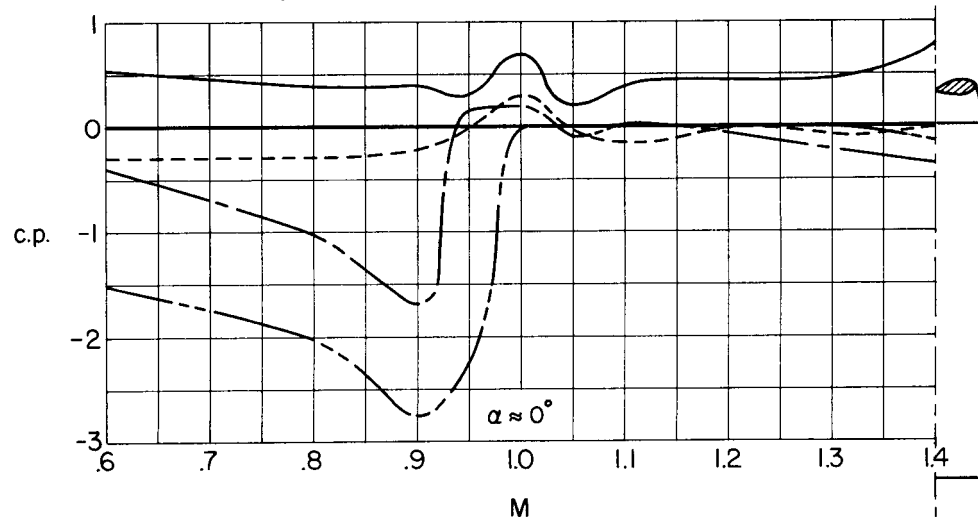
(a) Cylindrical-body models.

Figure 8.- Effects of nose cone angle on the center-of-pressure location.

Note : Curves have been deleted where flow hysteresis caused
significant differences for increasing and decreasing α
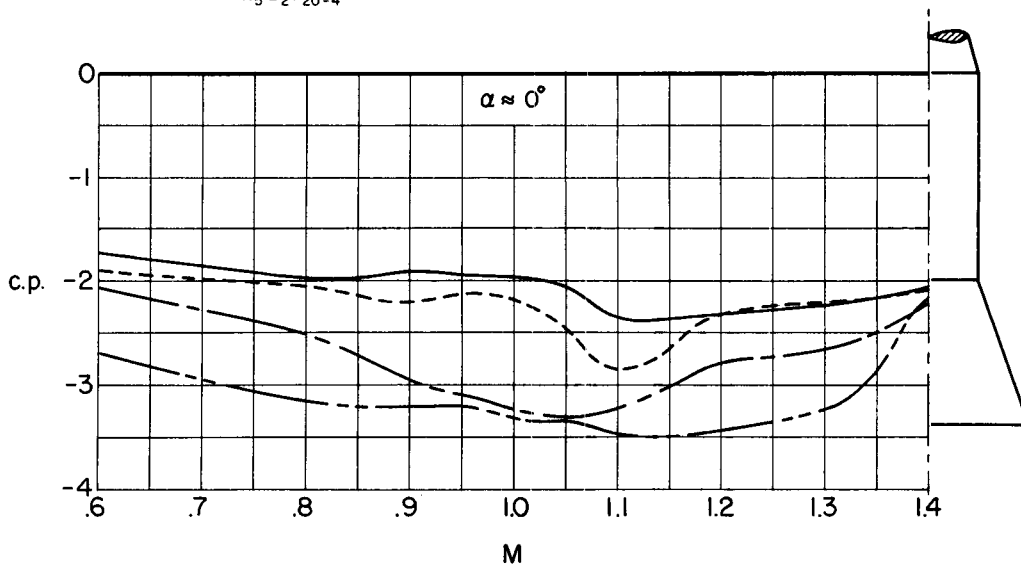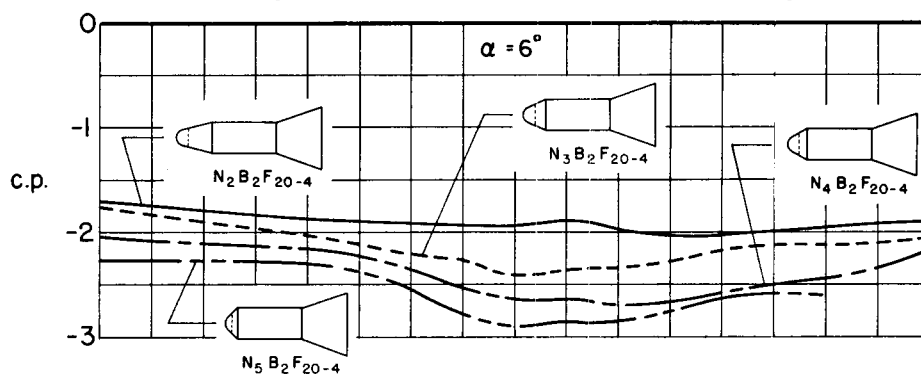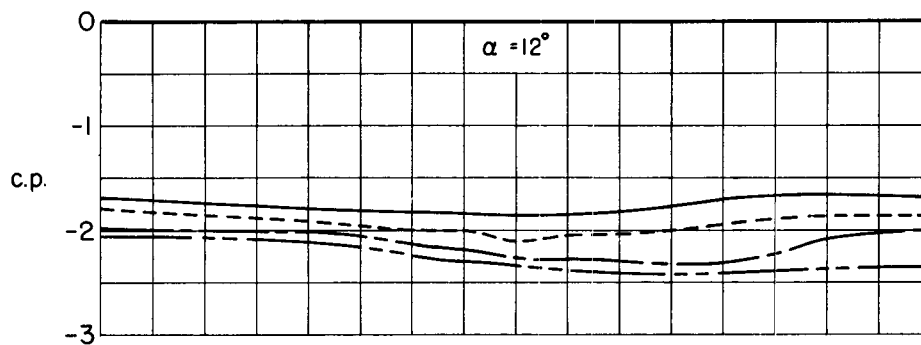
(b) Flared afterbody models.

Figure 8.- Continued.
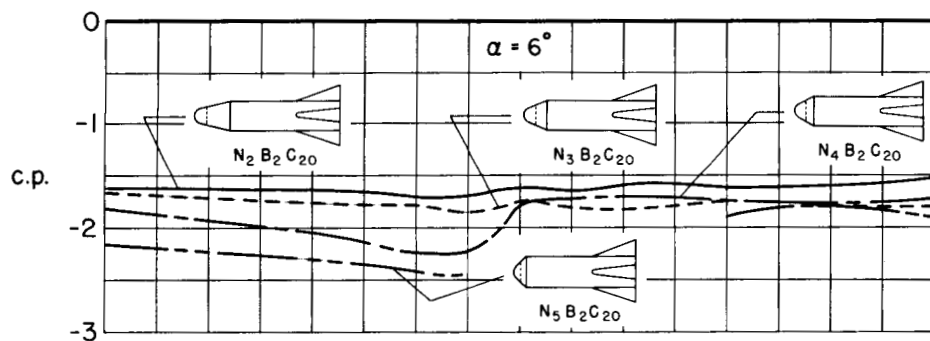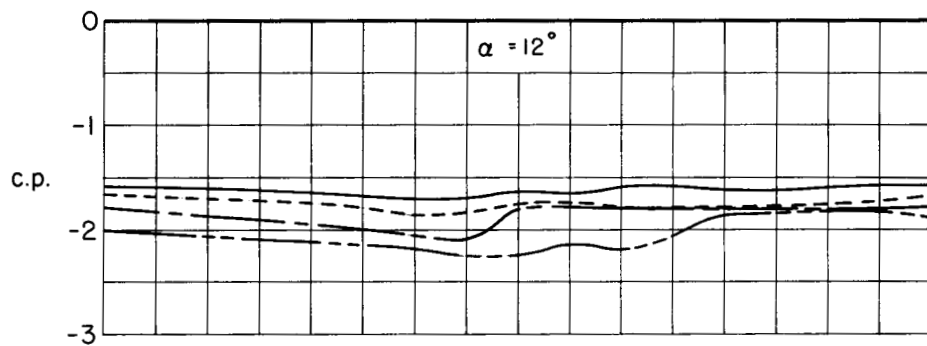
Note : Curves have been deleted where flow hysteresis caused significant differences for increasing and decreasing α
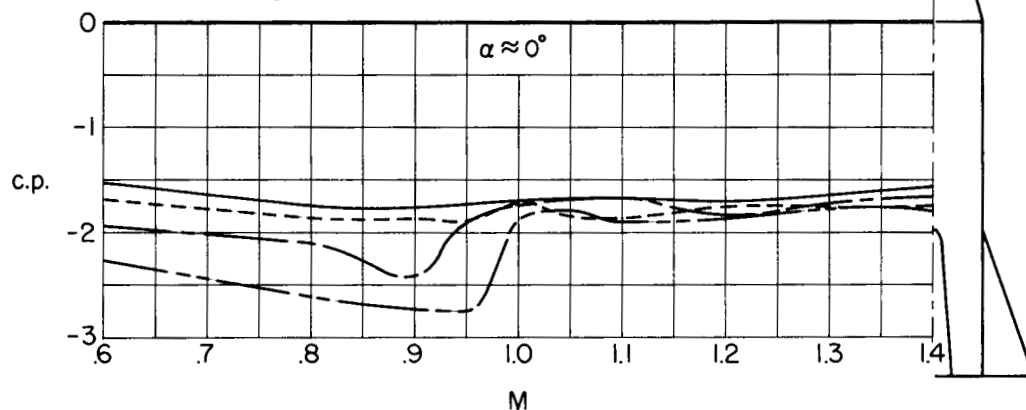
(c) Blunt-finned afterbody models.

Figure 8.- Concluded.
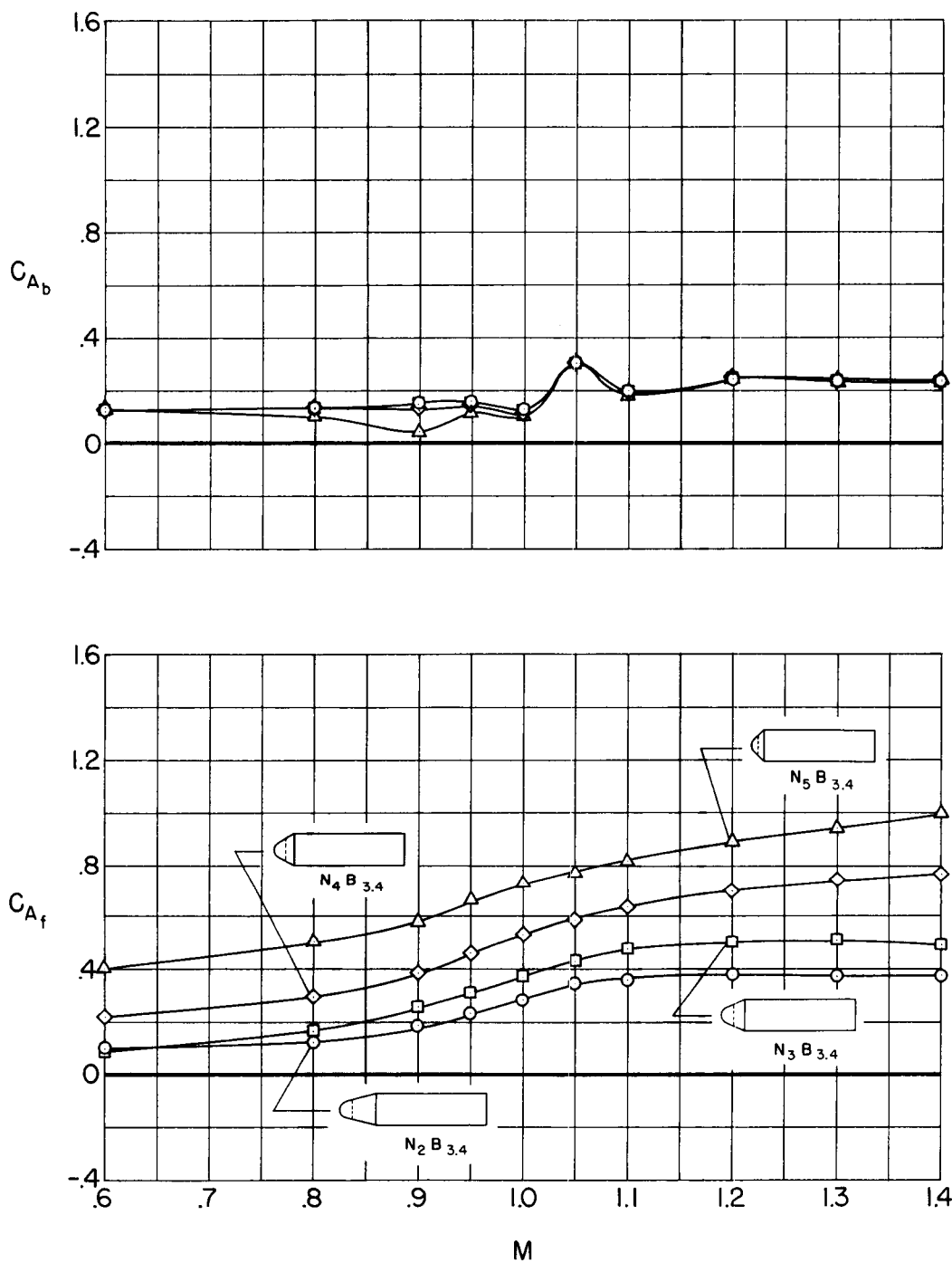
(a) Cylindrical-body models.

Figure 9.- Effects of nose cone angle on the forebody and base
axial-force coefficients.
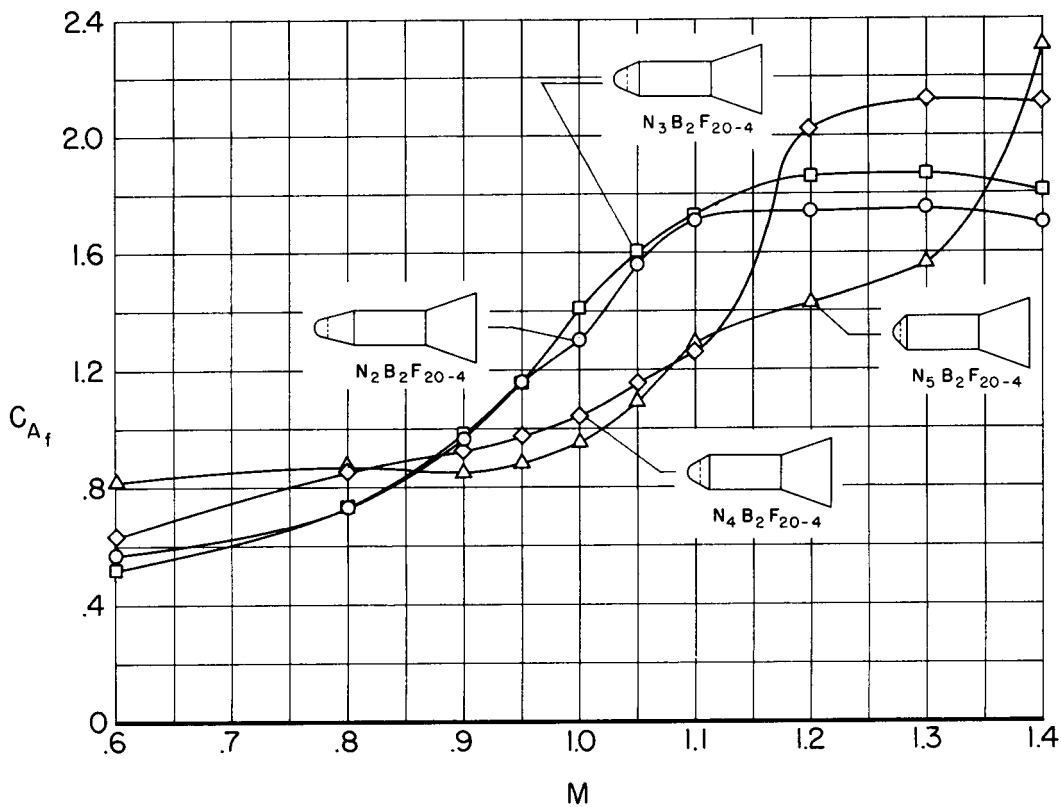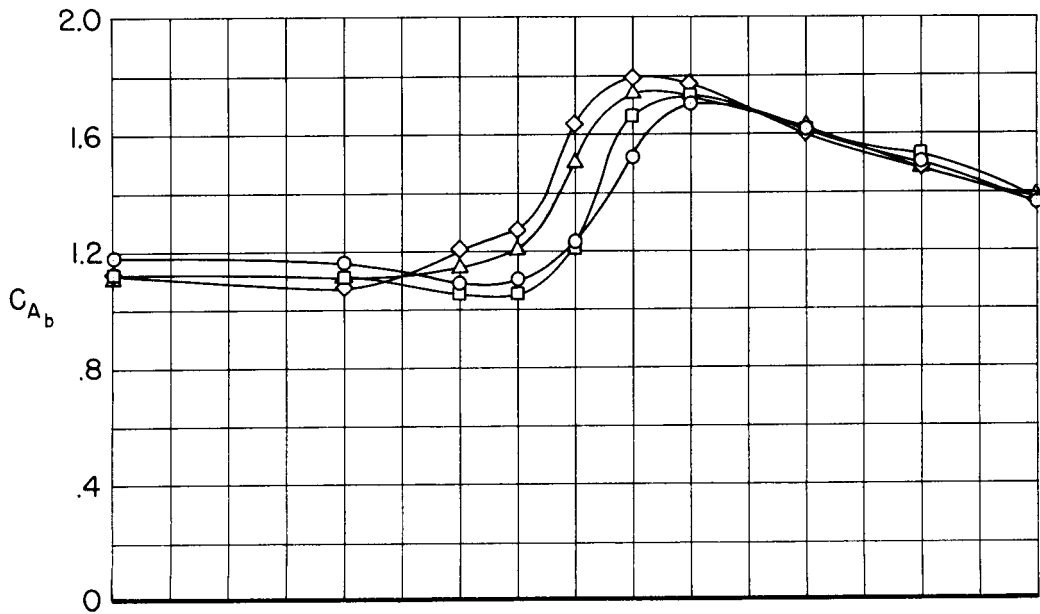
(b) Flared afterbody models.

Figure 9.- Continued.

A
4
2
8
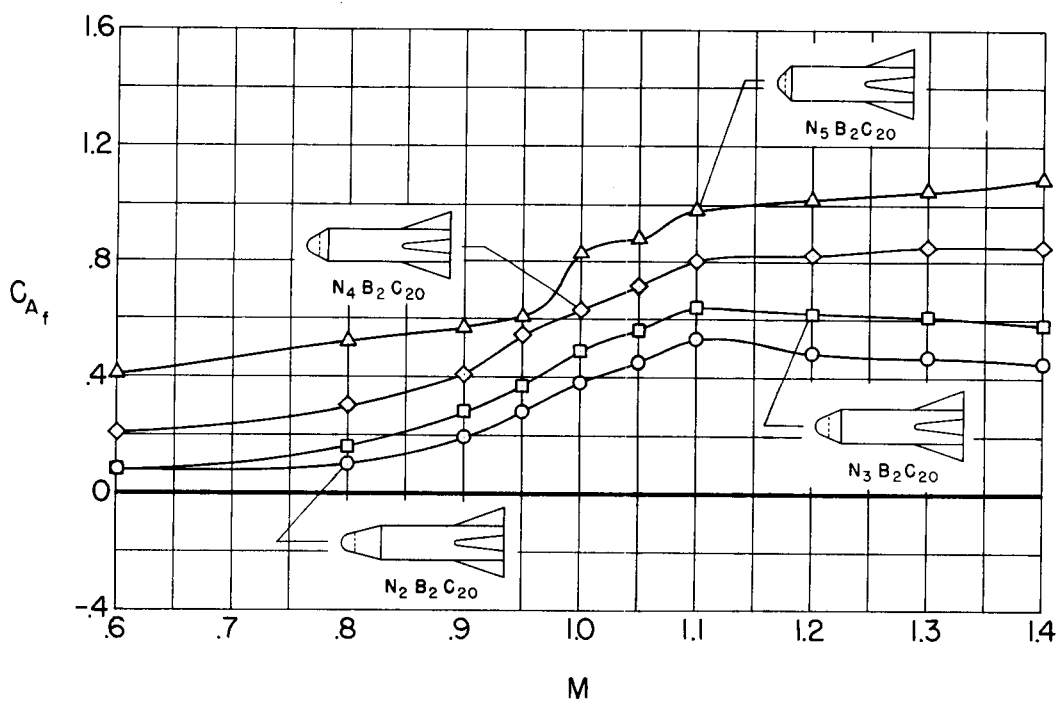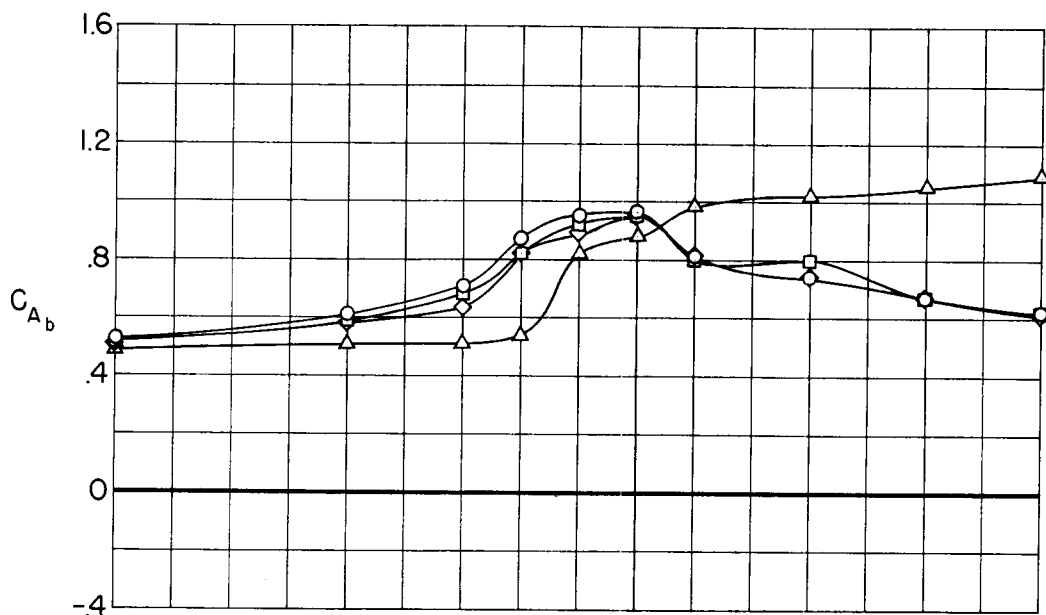
(c) Blunt-finned afterbody models.

Figure 9.- Concluded.

N₂B₃.₄

N₃B₃.₄

N₄B₃.₄

Boundary-layer trip wire

Balance shroud

N₅B₃.₄

Test section porous strip

A
4
2
8
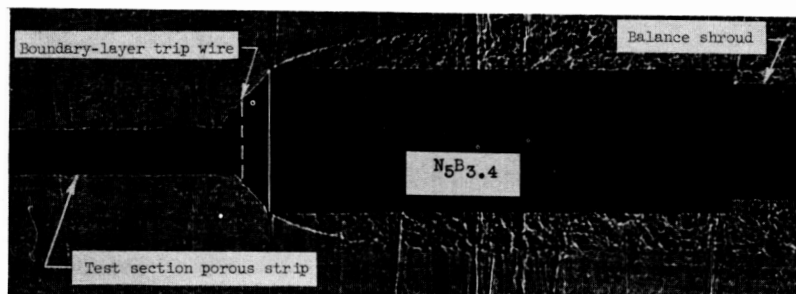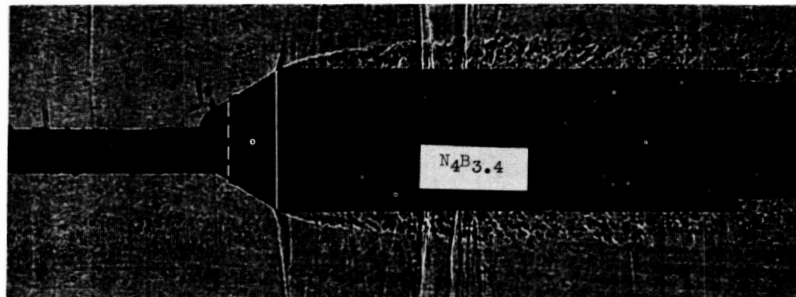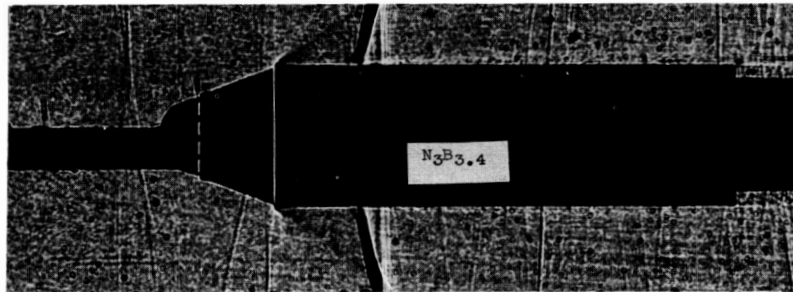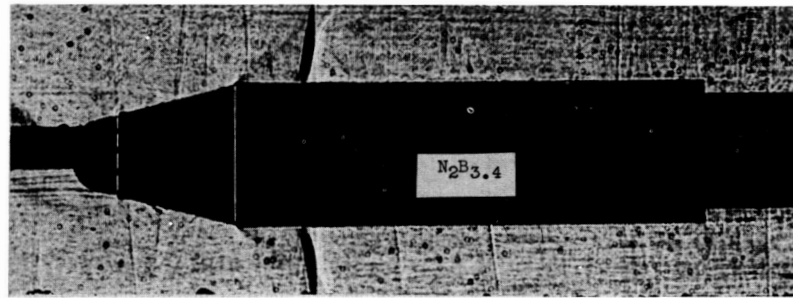
(a) M = 0.9

Figure 10.- The effects of nose cone angle on the flow patterns for the
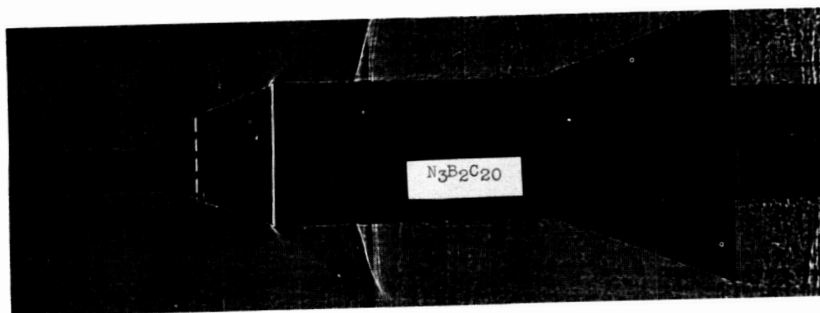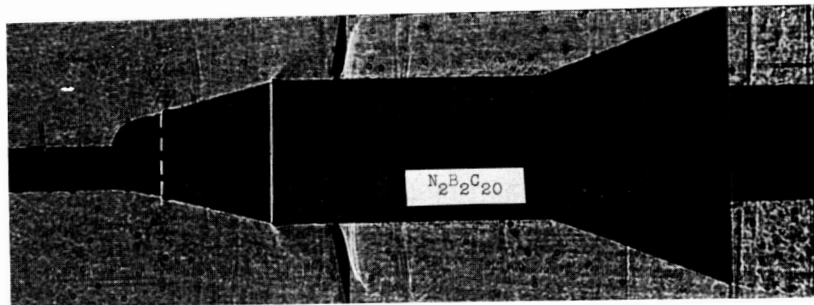models with a cylindrical afterbody at α=0°.
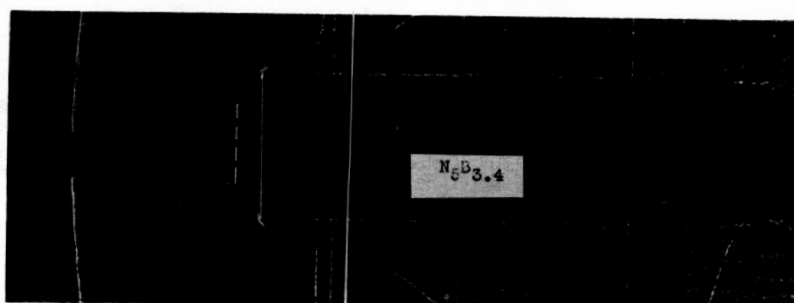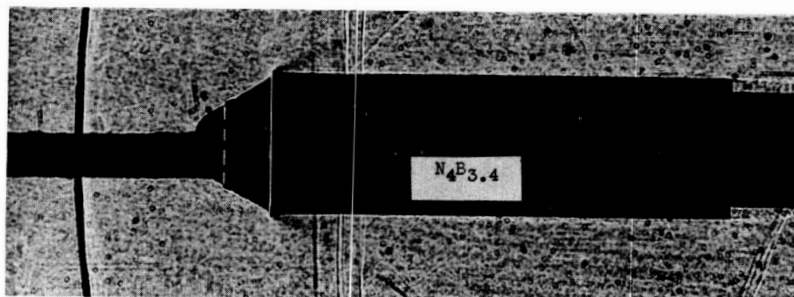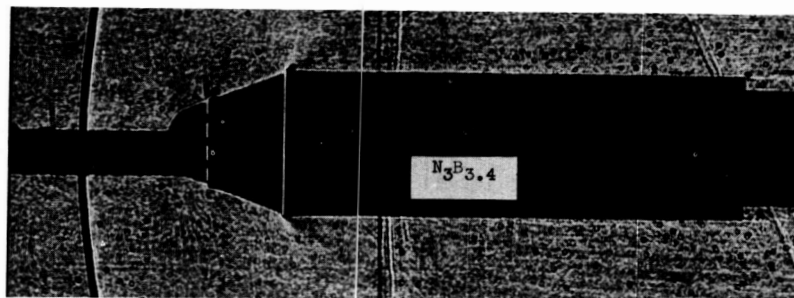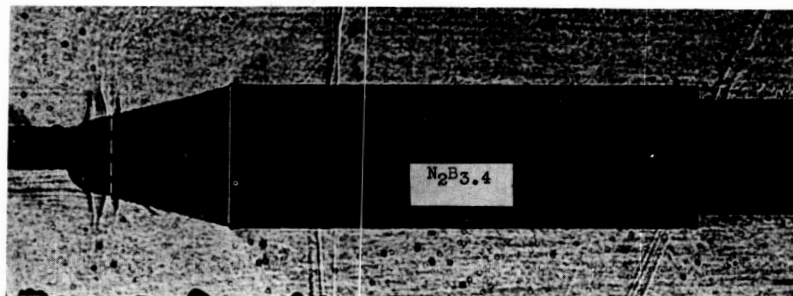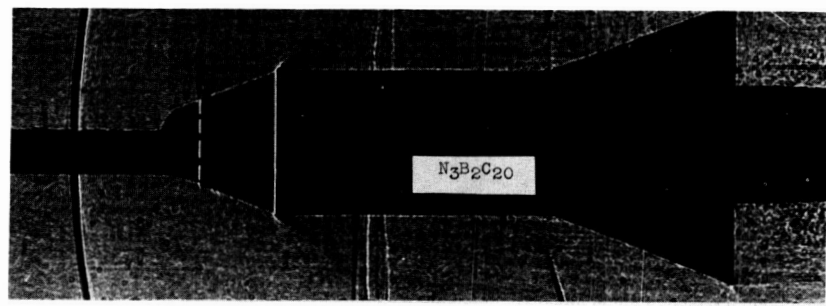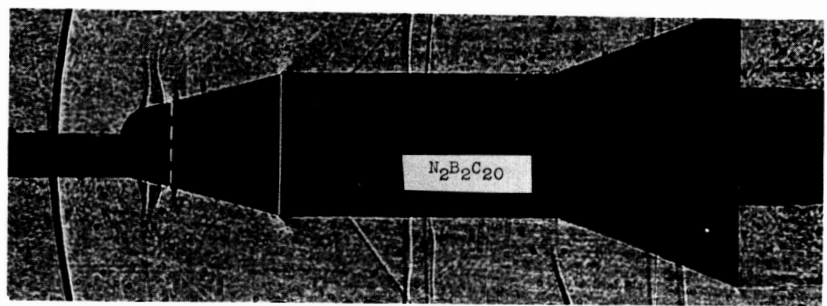
(b) M = 1.1

Figure 10.- Continued.
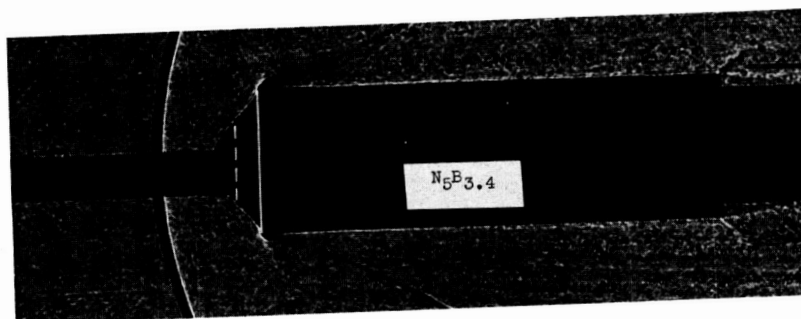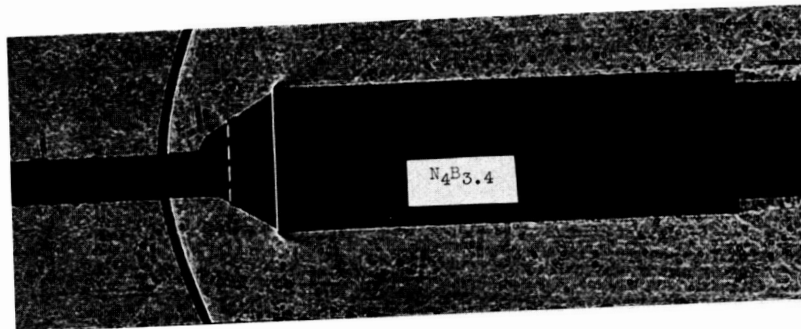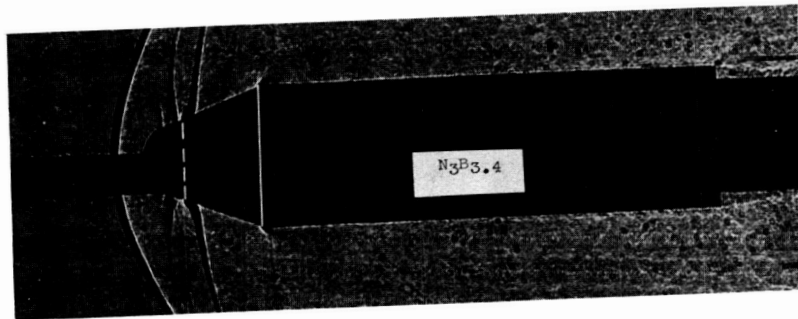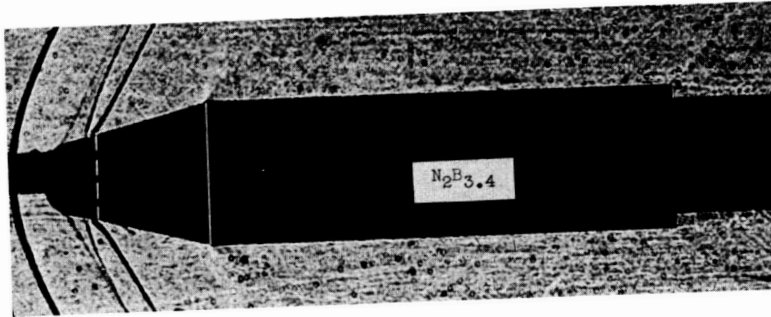
(c) M = 1.3

Figure 10.- Concluded.
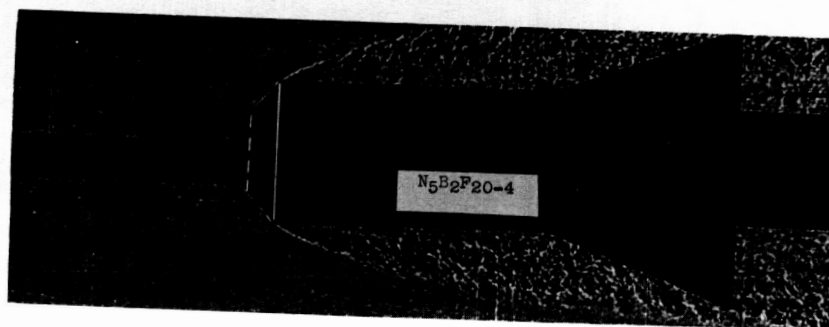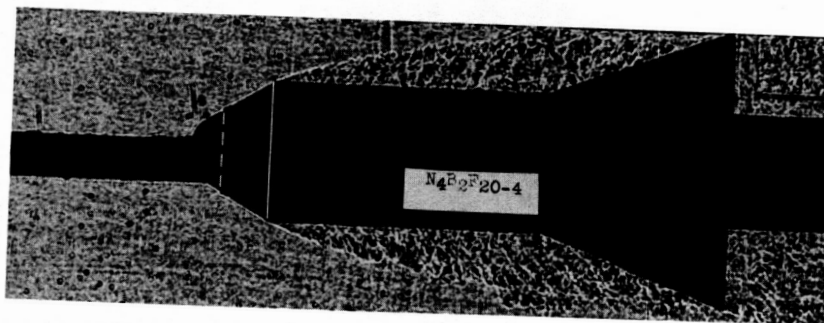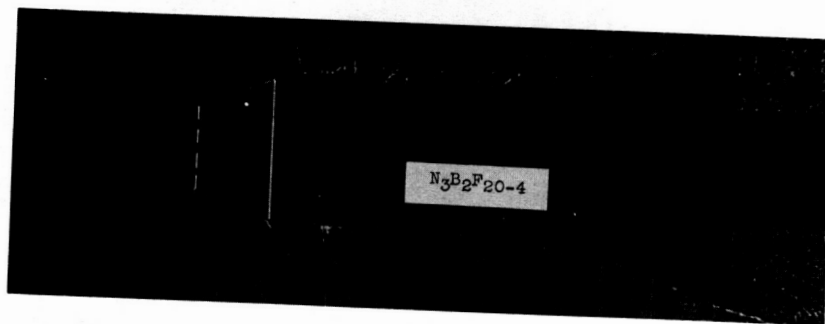
(a) M = 0.9

Figure 11.- The effects of nose cone angle on the flow patterns for the models with a flared afterbody at $\alpha = 0^\circ$.

N_2B_2F20-4

N_3B_2F20-4

N_4B_2F20-4

N_5B_2F20-4
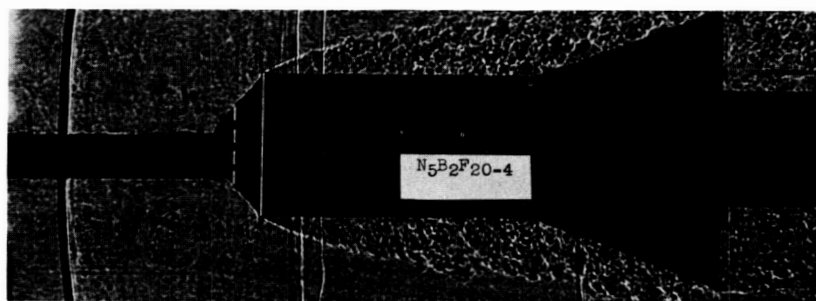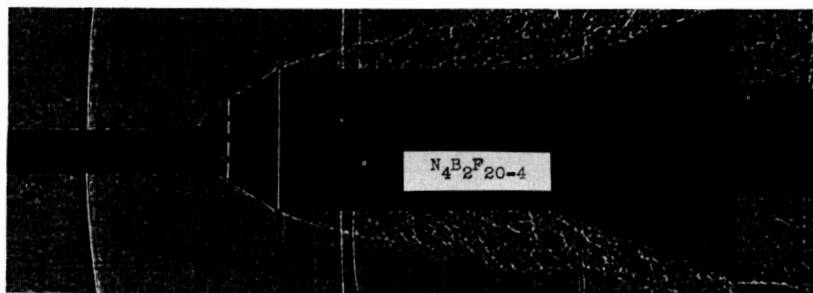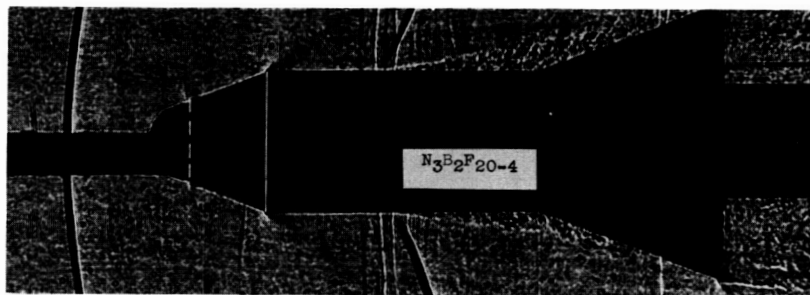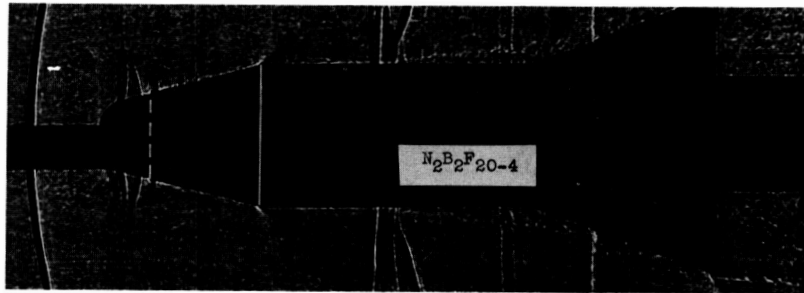
(b) M = 1.1

Figure 11.- Continued.
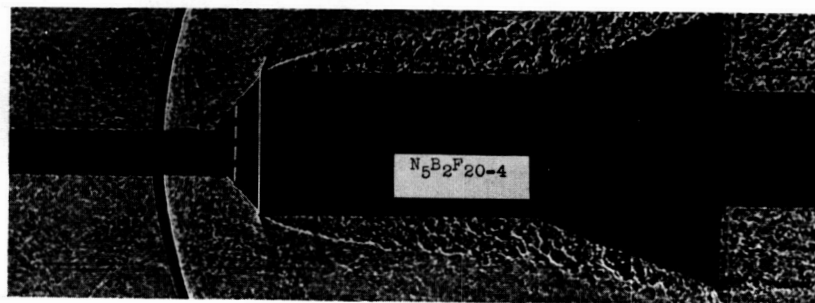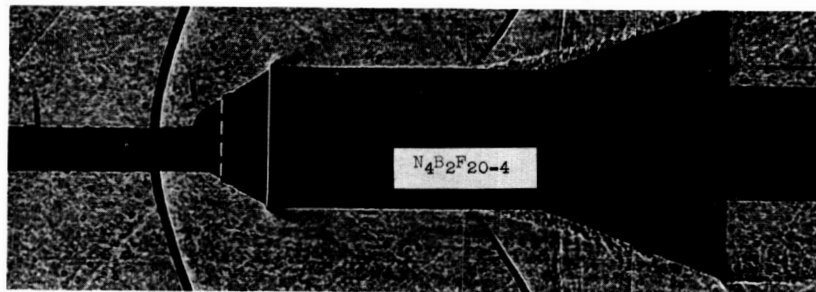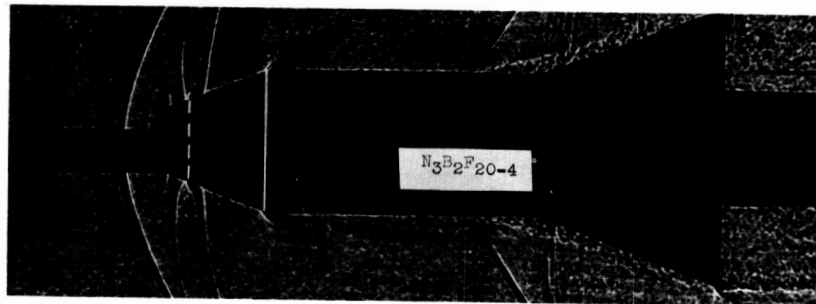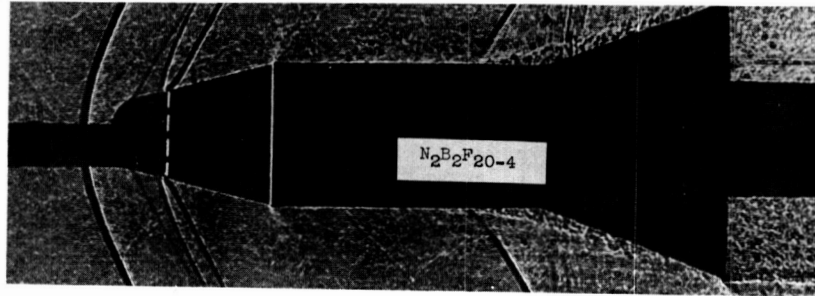
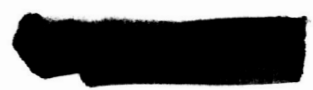(c) M = 1.3

Figure 11.- Concluded.

A
4
2
8
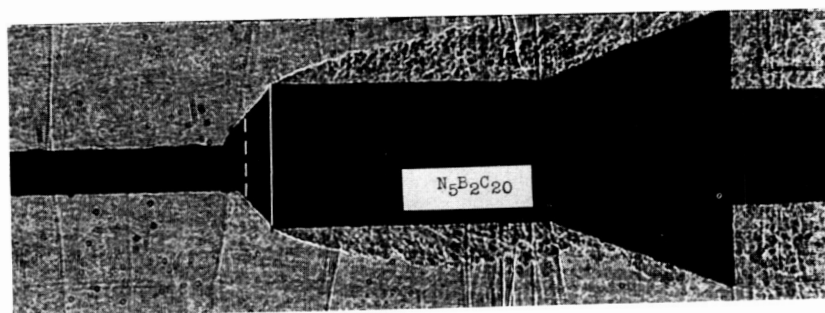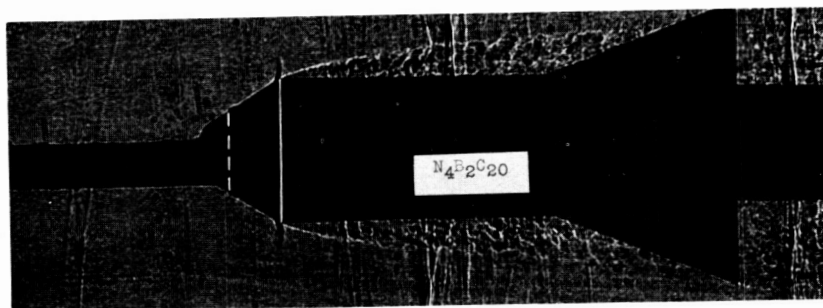
(a) M = 0.9

Figure 12.- The effects of nose cone angle on the flow patterns for the models with a blunt-finned afterbody at $\alpha=0^\circ$.
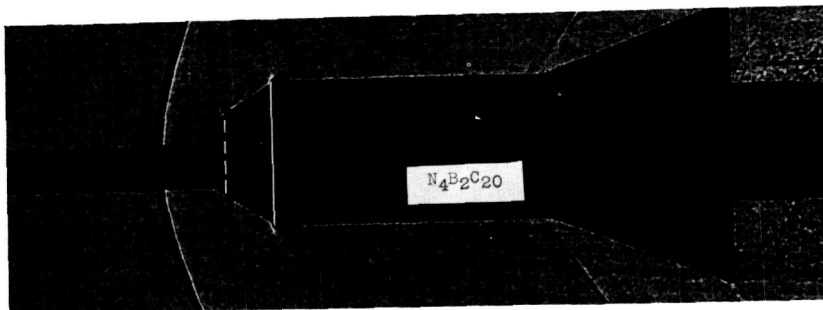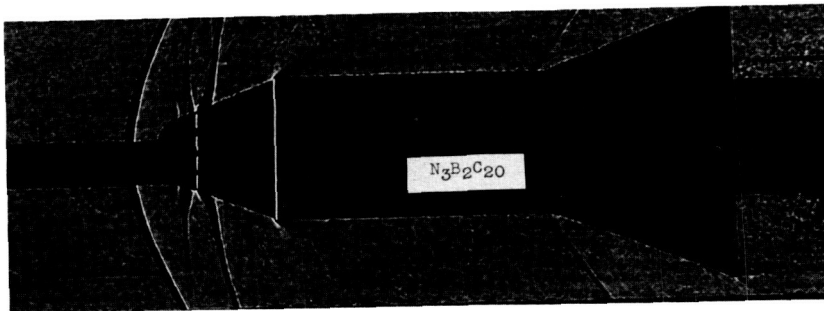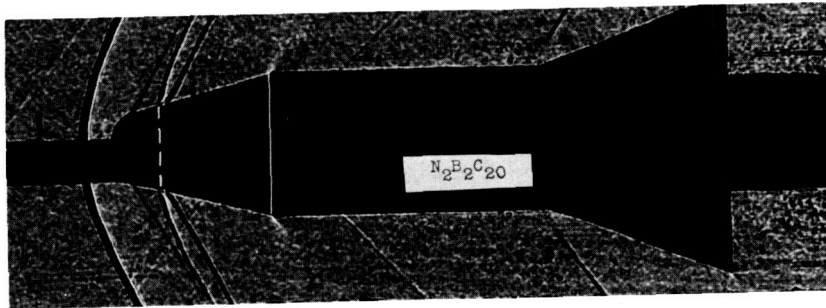
A
4
2
8
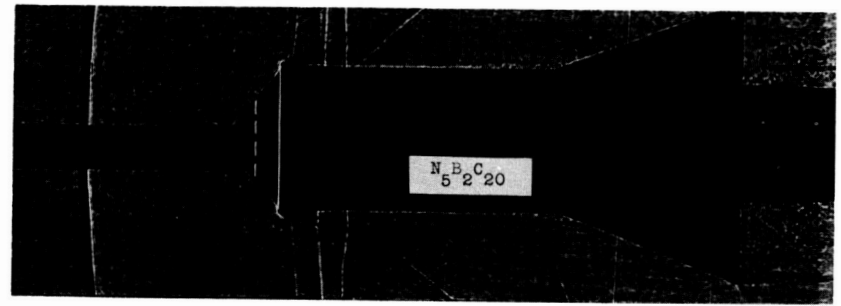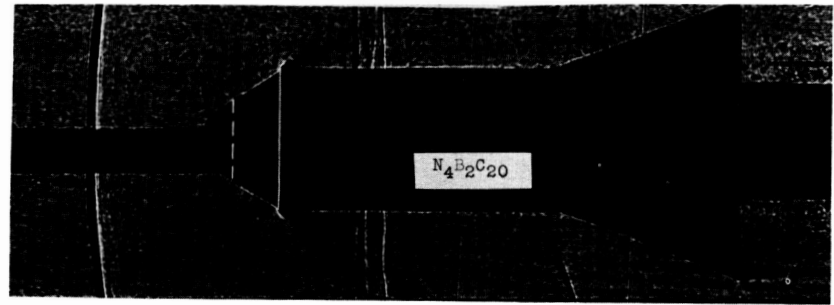
(b) M = 1.1

Figure 12.- Continued.

$N_2B_2C_{20}$

$N_3B_2C_{20}$

$N_4B_2C_{20}$

(c) M = 1.3

Figure 12.- Concluded.